[79] Thorsett S. E., Deich, W. T. S., Kulkarni, S. R., Navarro, J. and Vasisht, G. 1993, ApJ, 416, 182

[80] Thorsett, S. E. & Chakrabarty, D. 1999, ApJ, 512, 288

[81] Urpin, V., Geppert, U. and Konekov, D. 1998, A&A, 331, 244

[82] van den Heuvel, E. P. J., & van Paradijs, J. 1988, Nature, 334, 227

[83] van den Heuvel, E. P. J. & Lorimer. D. R. 1996, MNRAS, 283, L37

[84] van den Heuvel, E. P. J., & van Paradijs, J. 1997, ApJ, 483, 399

[85] Weisberg, J. M. & Taylor, J. H. 2002, ApJ, 576, 942

[86] Weisberg, J. M. & Taylor, J. H. 2003, Radio Pulsars, ASP Conference Series, 302, 93

[87] Will, C. 1992, Nature, 355, 111

[88] Wolszczan, A. 1991, Nature, 350, 688

[89] Wolszczan, A. & Frail, D. A. 1992, Nature, 355, 145

Contents

[61] Pacini, F. 1967, Nature, 216, 567

[62] Phillips, J. A. & Thorsett, S. E. 1994, Ap&SS, 212, 91

[63] Phinney, E. S., Evans, C. R., Blandford, R. D. and and Kulkarni, S. R. 1988, Nature, 333, 832

[64] Phinney, E. S. 1991, ApJ, 380, L17

[65] Phinney, E. S. 1992, Philos. Trans. R. Soc. London A, 341, 39

[66] Phinney, E. S. & Hansen, B. M. S. 1992, Planets Around Pulsars, ASP Conference Series, 36, 321

[67] Phinney, E. S. & Kulkarni, S.R. 1994, ARA&A, 32, 591

[68] Robinson, C. R., Lyne, A. G.., Manchester, R. N., Bailes, M., D'Amico, N. and Johnston, S. 1995, MNRAS, 274, 547

[69] Serenelli, A. M., Althaus, L. G., Rohrmann, R. D., Benvenuto, O. 2001, MNRAS, 325, 607

[70] Shapiro, I. I. 1964, Phys. Rev. Lett., 13, 789

[71] Stairs, I. H., Thorsett, S. E., Taylor, J. H. and Wolszczan 2002, ApJ, 581, 501

[72] Staveley-Smith, L., Wilson, W. E., Bird, T. S., Disney, M. J., Ekers, R. D., Freeman, K. C., Haynes, R. F., Sinclair, M. W., Vaile, R. A., Webster, R. L. and Wright, A. E. 1996, PASA, 13, 243

[73] Taylor, J. H. 1974, A&A, 15, 367

[74] Taylor, J. H., Fowler, L. A. and McCulloch, P. M. 1979, Nature 277, 437

[75] Taylor, J. H. & Weisberg, J. M. 1989, ApJ, 345, 434

[76] Taylor, J. H. & Cordes, J. M. 1993, ApJ, 411, 674

[77] Taylor, J. H. 1992, Phil. Trans. Royal Soc. of London, 341, 117

[78] Thorne, K. S. & Cutler, C. 2002, General Relativity and Gravitation, World Scientific, 72

[48] Lommen, A.N., Zepka, A., Backer, D. C., McLaughlin, M. A., Cordes, J. M., Arzoumanian, Z. and Xilouris, K. 2000, ApJ, 545, 1007

[49] Lorimer, D. R., McLaghlin, M. A., Arzoumanian, Z., Xilouris, K. M., Cordes, J. M., Lommen, A. N., Fruchter, A. S., Chandler, A. M. and Backer, D. C. 2004, MNRAS, 347, L21

[50] Lyne, A. G., Manchester, R. N., Lorimer, D. R., Bailes, M., D'Amico, N., Tauris, T. M., Johnston, S., Bell, J. F. and Nicastro, L. 1998, MNRAS, 295, 743

[51] Lyne, A. G., Burgay, M., Kramer, M., Possenti, A., Manchester, R. N., Camilo, F., McLaughlin, M. A., Lorimer, D. R., D'Amico, N., Reynolds, J., Freire, P. C. C. 2004, Science, 303, 1153

[52] Lyutikov, M. 2004, MNRAS submitted

[53] Manchester, R. N., Lyne, A. G., D'Amico, N., Bailes, M., Johnston, S., Lorimer, D. R., Harrison, P. A., Nicastro, L. and Bell, J. F. 1996, MNRAS, 279, 1235

[54] Manchester, R. N., Lyne, A. G., Camilo, F., Bell, J. F., Kaspi, V. M., D'Amico, N., McKay, N. P. F., Crawford, F., Stairs, I. H., Possenti, A., Kramer, M. and Sheppard, D. C. 2001, MNRAS, 328, 17

[55] Manchester, R. N. & Taylor, J. H. 1974, ApJ, 191, L63

[56] McLaughlin, M. A., Camilo, F., Burgay, M., D'Amico, N., Joshi, B. C., Kramer, M., Lorimer, D. R., Lyne, A. G., Manchester, R. N. and Possenti, A. 2004, ApJ, accepted

[57] Miri M. J. & Bhattacharya D. 1994, MNRAS, 269, 455

[58] Mitra, D. & Ramachandran, R. 2001, A&A, 370, 586

[59] Morris, D. J., Hobbs, G., Lyne, A. G., Stairs, I. H., Camilo, F., Manchester, R. N., Possenti, A., Bell, J. F., Kaspi, V. M., D'Amico, N., McKay, N. P. F., Crawford, F. and Kramer, M. 2002, MNRAS, 335, 275

[60] Nice, D. J., Arzoumanian, Z. and Thorsett, S. E. 2000, Pulsar Asronomy - 2000 and Beyond, ASP Conference Serie, 202, 67

Introduction

The Parkes High-Latitude Pulsar Survey is a survey covering a strip of the southern sky perpendicular to the galactic plane up to high latitudes ($b = \pm 60°$). It has been conceived and designed in the aim of increasing the sample of known millisecond pulsars (old neutron stars recycled to millisecond periods by a binary companion: §1.3) and detecting exotic binaries.

Large-scale pulsar surveys, particularly the Parkes Multibeam Pulsar Survey (pksmb, Manchester et al. 2001) have been very successful at discovering young, long-period pulsars. However, these surveys have found very few millisecond pulsars; in fact, of the almost 1600 pulsars now known in the galactic disk, only ~ 50 are millisecond pulsars, (another ~ 50 have been observed in globular clusters) despite the fact that the Galaxy is expected to contain roughly equal numbers of long-period and millisecond pulsars (Lyne et al. 1998). This discrepancy is due partly to the effects of interstellar dispersion and scattering (§1.4.1, 1.4.2), which decrease the detectability of short-period millisecond pulsars far more than their long-period counterparts. Furthermore, the long lifetimes of millisecond pulsars have allowed them to migrate away from the Galactic plane, where the pksmb and most other surveys were concentrated. Additionally, millisecond pulsars generally have lower luminosity than their long-period counterparts, resulting in a flux-density-limited distribution extending to high Galactic latitudes (Lyne et al. 1998). Johnston and Bailes (1991) and Thorsett et al. (1993) have argued that the observed spatial distribution of millisecond pulsars is consequently isotropic.

For these reasons, high-latitude searches as the one presented in this work, are the optimal strategy for finding more millisecond pulsars.

It is worth noting that most of the exotic millisecond pulsar binary systems are found at high galactic latitudes. For instance the double neutron star binary PSR B1534+12 has a latitude of 48 degrees (Wolszczan 1991) and the "planet pulsar" B1257+12 is located at a latitude of 75 degrees (Wolszczan

& Frail 1992). Moreover, the recently discovered isolated millisecond pulsar J0030+0451 (Lommen et al. 2000) has been found at a latitude of -60 degrees. These isolated millisecond pulsars are also very interesting, allowing us to test theories of how such objects may have lost their binary companions (evaporation, supernova kicks...).

Scientific Goals

Discovering more millisecond pulsars allow to address many interesting physical and astrophysical issues such as

- **General Relativity:** due to the high stability of their periodic signal and thanks to the precision with which we can measure the times of arrival of their pulses, millisecond pulsars with compact massive companions are excellent laboratories for tests of relativistic gravity (see §4.3.1). The interaction of two massive bodies, separated by at most few solar radii, leads to significant deviations from the keplerian laws of motion. Moreover, a distortion of the space-time around the pulsar due to the presence of a massive body modifies the path followed by the clocklike radio signals inducing a change in the measured times of arrival of the pulses.

- **NS Equation of State:** finding pulsars with periods shorter than the shortest-known period of 1.56-ms (Backer et al. 1982) would be crucial for constraining the neutron star equations of state (EoS, Cook et al. 1994). The smallest possible spin period reachable by a rotating neutron star can be roughly estimated imposing that the gravitational force is equal to the centrifugal force at the breakup limit. This simple assumption gives a limit spin period $P_{min} \propto R^{9/4}M^{-1/2}$. Different EoS give a different relation between masses and radii, hence, through detailed calculations, to a different value of P_{min}.

- **Millisecond Pulsar Timing Array:** the aforementioned stability of millisecond pulsars enables us in principle to detect any kind of distortion introduced in the highly predictable times of arrival (TOAs) of their pulses. The passage of a gravitational wave (produced e.g. by the coalescence of two neutron stars or two black holes) would distort the space-time and produce a change in the path followed by the radio waves

[34] Hewish, A., Bell, S. J., Pilkington, J. D. H.,Scott, P. F. and Collins, R. A. 1968, Nature, 217, 709

[35] Hobbs, G., Faulkner, A., Stairs, I. H., Camilo, F., Manchester, R. N., Lyne, A. G., Kramer, M., D'Amico, N., Kaspi, V. M., Possenti, A., McLaughlin, M. A., Lorimer, D. R., Burgay, M., Joshi, B. C. and Crawford, F. 2004, submitted to MNRAS

[36] Hulse, R. A. & Taylor, J. H. 1975, ApJ, 195, L51

[37] Jacoby, B. A. 2003, Radio Pulsars, ASP Conference Series, 302, 133

[38] Johnston, S. & Bailes, M. 1991, MNRAS, 252, 277

[39] Joshi, B. C. & Vivekanand, M. 2000, MNRAS, 316, 716

[40] Kalogera, V., Narayan, R., Spergel, D. N. and Taylor, J. H. 2001, ApJ, 556, 340

[41] Kalogera, V., Kim, C., Lorimer, D. R., Burgay, M., D'Amico, N., Possenti, A., Manchester, R. N., Lyne, A. G., Joshi, B. C., McLaughlin, M. A., Kramer, M., Sarkissian, J. M. and Camilo, F. 2004, ApJ, 601, L179

[42] Kaspi, V. M., Lyne, A. G., Manchester, R. N., Crawford, F., Camilo, F., Bell, J. F., D'Amico, N., Stairs, I. H., McKay, N. P. F., Morris, D. J., Possenti, A. 2000, ApJ, 543, 321

[43] Kim, C., Kalogera, V. and Lorimer, D. R. 2003, ApJ, 584, 985

[44] Kluzniak, W., Ruderman, M., Shaham, J., Tavani, M. 1988, Nature, 334, 225

[45] Kramer, M. 1998, ApJ, 509, 856

[46] Kramer, M., Xilouris, K. M., Lorimer, D. R., Doroshenko, O., Jessner, A., Wielebinski, R., Wolszczan, A. and Camilo, F. 1998, ApJ, 501, 270

[47] Kramer, M., Bell, J. F., Manchester, R. N., Lyne, A. G., Camilo, F., Stairs, I. H., D'Amico, N., Kaspi, V. M., Hobbs, G., Morris, D. J., Crawford, F., Possenti, A., Joshi, B. C., McLaughlin, M. A., Lorimer, D. R., Faulkner, A.J. 2003, MNRAS, 342, 1299

[16] Camilo, F., Nice, D. J. and Taylor, J. H. 1996, ApJ, 461, 812

[17] Camilo, F., Nice, D. J., Shrauner, J. A. and Taylor, J. H. 1996, ApJ, 469, 819

[18] Camilo, F., Lorimer, D. R., Freire, P., Lyne, A. G. and Manchester, R. N. 2000, ApJ, 535, 975

[19] Camilo, F., Lyne, A. G., Manchester, R. N., Bell, J. F., Stairs, I. H., D'Amico, N., Kaspi, V. M., Possenti, A., Crawford, F., McKay, N. P. F. 2001, ApJ, 548, L187

[20] Caron, B. et al. 1997, Nucl. Phys., B54, 167

[21] Cheng, K. S. 1987, ApJ, 321, 799

[22] Cheng, K. S. 1987, ApJ, 321, 825

[23] Cocke, W. J., Disney, M. J. and Taylor, D. J. 1969, Nature, 221, 525

[24] Condon, J. J., Cotton, W. D., Greisen, E. W., Yin, Q. F., Perley, R. A., Taylor, G. B. and Broderick, J. J. 1998, AJ, 115, 1693

[25] Cook, G. B., Shapiro, S. L. and Teukolsky, S. A. 1994, ApJ, 424, 823

[26] Cordes, J. M. & Helfand, D. J. 1980, ApJ, 239, 640

[27] D'Alessandro, F., McCulloch, P. M., Hamilton, P. A. and Deshpande, A. A. 1995, MNRAS, 277, 1033

[28] Damour, T. & Deruelle, N. 1986, Ann. Inst. H. Poincaré (Physique Théorique), 44, 263

[29] Damour, T. & Taylor, J. H. 1992, Phys. Rev. D, 45, 1840

[30] Danzmann, K. et al. 1995, First Edoardo Amaldi Conference on Gravitational Wave Experiments, World Scientific, 100

[31] Edwards, R. T., Bailes, M., van Straten, W., Britton, M. C. 2001, MNRAS, 326, 358

[32] Hellings, R. W. & Downs, G. S. 1983, ApJ, 265, L39

[33] Hankins, T. H. & Rickett, B. J. 1975, Meth. Comp. Phys., 14, 55

from a pulsar to a radio telescope hence determining a measurable change in its TOAs. To catch such signal and to distinguish its signature from timing noise or other sources of uncertainties, (see §2.3.1) it is necessary to monitor the TOAs of many millisecond pulsars in different directions of the sky, creating a sort of timing array. Accumulating a larger sample of millisecond pulsars randomly distributed in space is then important in optimizing the performances of the array.

- **Binary Evolution:** Eclipsing millisecond pulsars, binaries where the radio signal is periodically eclipsed by plasma streaming off the companion (Nice et al. 2000), are a laboratory for understanding the evolution of low-mass neutron star binaries into isolated pulsars (see §3.2.1) and may also be important for understanding the formation of planets around pulsars (see e.g. Banit et al. 1993, Phillips and Thorsett 1994, Phinney & Hansen 1992).

- **Population Statistics:** A more accurate determination of the millisecond pulsar spatial distribution enables to set better constraints on the birth rate, origin and evolution of these objects. It also allows assessment of the still largely uncertain millisecond pulsar luminosity function and improves the knowledge of their velocity distribution, also related to formation mechanisms.

As evidenced by the results of the Swinburne intermediate-latitude pulsar surveys (Edwards et al. 2001, Jacoby 2003) any survey devoted to the discovery of millisecond pulsars will yield an even greater number of long-period pulsars. The long-period pulsars found at high latitudes are likely to be nearby or to be old enough or moving rapidly enough to have migrated from their birth sites in the Galactic plane. Finding these nearby, older, or high-velocity pulsars is important for understanding

- **Pulsar Velocities:** Determining the shape of the high-velocity tail of the pulsar velocity distribution puts constraints on the physics of the "kick" imparted to the neutron star during its supernova explosion (van den Heuvel & van Paradijs 1997, Burrows 1998). It is also relevant in assessing the retention of neutron stars in globular clusters.

- **Pulsar Ages:** Better determining the pulsar age distribution helps in understanding the evolution of the luminosity function, magnetic field

and, radio emission processes of the pulsar population.

- **Emission Mechanisms:** Older pulsars are more likely to exhibit phenomena such as 'nulling' or 'drifting subpulses' (Joshi & Vivekanand 2000), unique diagnostics of radio emission mechanisms.
- **Local Interstellar Medium:** Finding nearby and high-latitude pulsars is important for modelling the distribution of the interstellar material near the Sun.

The Focus of the Thesis

The survey observations have been completed in December 2003 and 95% of the data have been processed to date (15 March 2004). This thesis describes the characteristics of the survey and presents the new discoveries whose number and nature matches, and in one case go beyond, the expectations according to which the survey had been undertaken.

Many of the investigations mentioned in the previous section requires collecting observations of the new discoveries for at least one year and in some cases few years (pulsar ages, population statistics, pulsar velocities, millisecond pulsar timing array) and hence are still works in progress at the time of the delivery of this thesis.

In chapter 1 a review of the basic knowledge on pulsars is presented, briefly treating their discovery, emission mechanism, evolution and observational properties. Chapter 2 describes the technical characteristics of the survey object of this work, the data acquisition and analysis and the follow-up data treatment (confirmations and timing of new discoveries). In §3 the results of the Parkes High-Latitude survey (discoveries and timing solutions, when available) are reported, with particular attention to the newly discovered millisecond pulsars. Finally, §4 focuses on the most important result of this work: the discovery of the first double pulsar system, PSR J0737−3039A/B, and on the implications that its discovery has in many fields of physics and astrophysics. In particular §4.3.1 shows the importance of the timing of the two pulsars in this binary system for testing General Relativity and relativistic gravity, §4.3.2 describes the impact that this discovery has on the determination of the Double Neutron Stars (DNSs) merger rate and, by implication, on the possibility to detect gravitational wave bursts produced

Bibliography

[1] Abramovici, A., Althouse, W. E., Drever, R. W. P., Gursel, Y., Kawamura, S., Raab, F. J., Shoemaker, D., Sievers, L., Spero, R. E., Thorne, K. S. 1992, Science, 256, 325

[2] Alpar, M. A., Cheng, A. F., Ruderman, M. A. and Shaham, J. 1982, Nature, 300, 728

[3] Alpar, M. A., Nandkumar, R. and Pines, D. 1986 , ApJ, 311, 197

[4] Arzoumanian, Z., Fruchter, A.S. and Taylor, J. H. 1994, ApJ, 426, L85

[5] Aerzoumanian, Z., Cordes, J. M. and Wasserman, I. 1999, ApJ, 520, 696

[6] Baade, W. & Zwicky, F. 1934, Phys. Rev., 45, 138

[7] Backer, D. C., Kulkarni, S. R., Heiles, C., Davis, M. M. and Goss, W. M. 1982, Nature, 300, 615

[8] Banit, M., Ruderman, M. A., Shaham, J. and Applegate, J. H. 1993, ApJ, 415, 779

[9] Becker & Trümper 1999, A&A, 341, 803

[10] Bhattacharya, D., van den Heuvel, E. P. J. 1991, Phis. Rev., 203, 1

[11] Blandford, R., Teukolsky, S. A. 1976, ApJ, 205, 580

[12] Burderi, L., King, A. R. and Wynn, G. A. 1996, ApJ, 457, 351

[13] Burgay, M., D'Amico, N., Possenti, A., Manchester, R. N., Lyne, A. G., Joshi, B. C., McLaughlin, M. A., Kramer, M., Sarkissian, J. M., Camilo, F., Kalogera, V., Kim, C. and Lorimer, D. R. 2003, Nature, 426, 531

[14] Burrows, A. 1998, Nature, 393, 121

[15] Camilo, F., Nice, D. J. and Taylor, J. H. 1993, ApJ, 412, L37

during the merging of the two stars in such systems. Section 4.3.3 highlights the so-far unique emission characteristics of the pulsars in this system (in particular of the so-called pulsar B) showing how these observations open the possibility to test for the first time the pulsars' magnetospheres and interactions between magnetic fields and pulsar's energy outflow.

Acknowledgments

I would like to thank my supervisor, Roberto Fanti, who guided my first steps in astronomy and who introduced me to the fabulous world of pulsars. Many thanks to my co-supervisors Andrea Possenti, Nichi D'Amico and Andrew Lyne for their invaluable help and support in the last three years.

I would also like to thank my collaborators of the 'PHsurv team' for their friendship and cooperation: I really enjoyed the days we spent together in Parkes and in Jodrell Bank. A special thank to Andy Faulkner who's been down-under with me in my last days as a PhD student and gave me moral support while I was completing this thesis; thanks to Janette for the material (edible) support.

And finally, very special thanks to my dearest friends Francy, Lorenzo, Piero (thanks for the DLTs!), Marcy, Elena, Luca A., Luca Z., Marcella, Cristian, Gianni, Matteo, Francesca, Andrea and Anna Lia. This eight years with you have been really special and I will miss you.

Chapter 1

Pulsars: Overview

1.1 A Brief History of Radio Pulsars

The first pulsar (*pulsating radio source*, Hewish et al. 1968) was discovered in 1967 by Jocelyn Bell, a research student at Cambridge University, and her supervisor Anthony Hewish (awarded with the Nobel prize for Physics in 1974), during an experiment on the interplanetary scintillation of extragalactic radio sources. The astronomical origin of the recorded signal, that strongly resembled terrestrial radio frequency interference (RFI), became clear when it was noticed that it reappeared four minutes earlier each day, as expected from a celestial source observed with a transit telescope.

This object showed extremely regular pulsations with a period of 1.337 s and lasting few hundredths of second. On the basis of the the so-called causality principle, stating that a signal of duration t must be emitted from a source with a diameter $d \leq t \times c$ (where c is the speed of light), it was argued that the object responsible for the radio pulsations should have a very small radius. At first, because of the small inferred size and of the regularity of the pulses, the hypothesis that this could be a signal from an extraterrestrial intelligence was taken into account and the first pulsar was nicknamed LGM1 (for Little Green Man 1). Very soon professor Hewish and Miss Bell understood that this couldn't be an artificial signal, firstly because three more similar recordings were found in different positions of the sky and secondly because there was no evidence of an orbital motion of the emitting object which would have been detected if it was a message coming from an extraterrestrial planet orbiting its sun.

The attention then moved to small sized stellar objects: white dwarfs, whose radius is about a few thousand kilometers, or neutron stars, whose

existence was postulated in 1934 (Baade & Zwicky 1934) but never observationally verified. The ultimate evidence that pulsars were indeed neutron stars came from the discovery, a year later, of the pulsar in the Crab Nebula (Cocke, Disney & Taylor 1969), a plerionic supernova remnant that Franco Pacini, before the discovery of the first radio pulsar (Pacini 1967) theorised that could be powered by a rotating magnetised neutron star. In fact, the short period of the Crab pulsar (only 33 milliseconds) ruled out the white dwarf hypothesis: at this rotational speed an object such that would be disrupted by the centrifugal force overwhelming the gravity. The observation of spin-down in this object (Richards 1969) also confirmed that the source of periodicity was indeed rotation and not vibration, as also theorised in the first years, for which slow down is not expected (Pacini 1968).

1.2 Radio Emission

Pulsars are highly magnetised rapidly rotating neutron stars (NSs). The origin of both the fast spinning and high magnetisation is not fully understood yet, but it is probably related to angular momentum and magnetic flux conservation during the supernova explosion that produces the neutron star. Since the magnetic axis is not aligned with the rotational axis the neutron star's dipole moment is time-varying and thus the star radiates a significant amount of energy in the form of electromagnetic waves at the rotation frequency Ω:

$$\dot{E}_{dipole} = -\frac{2B^2R^6\Omega^4\sin^2\alpha}{3c^3} \tag{1.1}$$

here B is the surface magnetic field, R is the radius of the NS (typically ~ 10 km) and α is the angle between the magnetic and the rotational axis. The energy emitted via magnetodipole radiation is supplied by the loss of rotational energy:

$$\dot{E}_{rot} = I\Omega\dot{\Omega} \tag{1.2}$$

where I is the moment of inertia of the star ($\sim 10^{45}$ g cm^2) and $\dot{\Omega}$ is the derivative of the spin frequency.

Equating the two expressions above we can obtain, assuming $\alpha = 90°$, an estimate of the surface magnetic field of the rotating neutron star in terms of its period $P = 2\pi/\Omega$ and the period derivative $\dot{P}$:

$$B = \sqrt{\frac{3c^3I}{8\pi^2R^6}P\dot{P}} \simeq 3.2 \times 10^{19}\sqrt{P\dot{P}} \qquad \mathrm{G} \tag{1.3}$$

investigate the related kick velocities (i.e. the one imparted to the pulsar in the supernova explosion).

A big observational and theoretical effort will be put, in the next years, in the study of the Double Pulsar system. Extended follow-up observations, at radio frequencies and in other spectral bands, are required in order to answer many of the questions raised by the discovery of J0737$-$3039 and by the puzzling behavior observed in the emission of the two pulsars harboured in this system. At present, along with the timing campaign at the Parkes radio telescope, VLBA observation are on-going with the aim to measure the parallactic distance of the system and its proper motion. Knowledge of these parameters will allow a precise determination of the contaminating effects of the galactic potential and of the proper motion itself on the measured value of the binary period derivative and will allow to measure the fifth post-keplerian parameter (the orbital decay) with unprecedented precision. Radio observations at various frequencies are also being performed with many different instruments (Effelsberg, GMRT, GBT radio telescopes) in order to assess the possible pulse shapes and emission characteristics variations with frequency. Also, polarimetric observation are on-going at the Parkes radio telescope aimed to the measurement of the geodetic spin-precession. These observations, monitoring the pulse shape and polarimetry variations with time, will allow to determine the geometry of the system and to predict the likely time at which the pulsed signals from each of the pulsars of this system could temporarily stop to cross our line of sight (Kramer 1998).

Optical observations with the Hubble Space Telescope, millimetric observations with the 30 m IRAM telescope and X-rays observations with XMM have also been proposed in order to study the multiwavelength behavior of the (pulsed and) unpulsed emission measured at radio frequencies and to try to understand its origin.

companion, possibly in the process of being ablated by the relativistic wind emitted by the pulsar (§3.2.1), while PSR J0900−3144 has a fairly massive companion, probably a Carbon-Oxigen white dwarf (§3.2.2).

The third, and by far more interesting, binary system found in the PH survey, is the one containing PSR J0737−3039A and PSR J0737−3039B. This is not only the most relativistic Double Neutron Star known (with an orbital velocity of 0.1% the speed of light), providing the best ever laboratory for testing General Relativity and implying an increase of almost an order of magnitude in the estimates of the DNSs coalescence rate (§4.3.2), it is also the first known Double Pulsar. The presence of a second detectable pulsation in such a system, providing the measurement of the mass ratio of the two stars, allows new and more precise tests for the theories of relativistic gravity (§4.3.1). Moreover, due to the close interaction between the two pulsars and to the high inclination of the orbit with respect to the line of sight, this system will also allow for the first time to map pulsars' magnetospheres and to have a better understanding of the processes that are generating the radio emission (§4.3.3).

5.1 On-Going and Future Work

Processing and inspection of the survey data is now complete at 95%. The last 5% of the data will be soon analysed and all the survey results will be re-examined using a new programme for displaying and selecting the suspects produced by the processing.

Timing of all the newly discovered pulsars and observations of new candidates are on-going at the Parkes radio telescope. Having a data span covering at least one year will ensure a precise determination of pulsars' positions and will allow follow-up observations at other wavelengths, most importantly X-rays and optical, especially for the millisecond pulsars (and their binary companions). Accurately knowing the position is crucial in order to obtain a reliable value of the spin down rate and hence of all its derived parameters, such as the characteristic age, the surface magnetic field and the spin-down energy. These quantities then, along with the observed ones, will be the basis for statistical studies on pulsar and millisecond pulsar populations. Collecting timing observations for an even longer data span will also give the possibility to measure proper motions, to study velocity distributions and to

The slow-down of pulsars is in general described by a relation $\Omega \propto \dot{\Omega}^n$, where n is the braking index (equal to 3 in the magneto-dipole model described above):

$$n = \frac{\Omega\ddot{\Omega}}{\dot{\Omega}^2} \tag{1.4}$$

Integrating the equation 1.4, if $n \neq 1$, we obtain an estimate of the age of the pulsar:

$$t = \frac{P}{(n-1)\,\dot{P}}\left[1 - \left(\frac{P_0}{P}\right)^{n-1}\right] \tag{1.5}$$

For $n = 3$ (dipole emission) and assuming that the initial spin period $P_0 \ll P$ we obtain the characteristic age τ of the pulsar:

$$\tau = \frac{P}{2\dot{P}} \tag{1.6}$$

According to the picture seen above, we can follow the evolution of an isolated pulsar (for pulsars in binary systems see §1.3) using the $P-\dot{P}$ diagram (fig. 1.1).

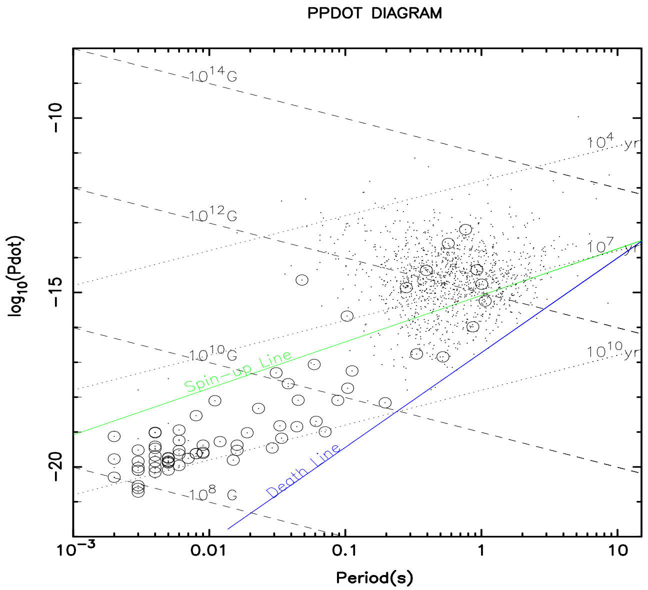

Figure 1.1: P–$\dot{P}$ diagram. The dashed lines denote constant magnetic fields, the dotted ones constant age, the green one is the spin-up line (see text) for an Eddington mass transfer rate and the blue line is the death line (see text). Circles denote the binary pulsars.

After the supernova explosion the pulsar is rapidly spinning and has a high magnetic field strength, hence, according to eq. 1.3, it has a high value of $\dot{P}$, placing it in the top-left side of the P–$\dot{P}$ diagram. As time passes the pulsar spins down and it moves rightwards in the diagram, following the constant B-field lines (or slightly turning downwards if the magnetic field decays). When the pulsar crosses the so-called *death-line*, the emission mechanism is no more efficient and the pulsar switches off. The exact location of this theoretical line in the P–$\dot{P}$ diagram depends on the details of the electrodynamical model adopted to explain the coherent radio emission.

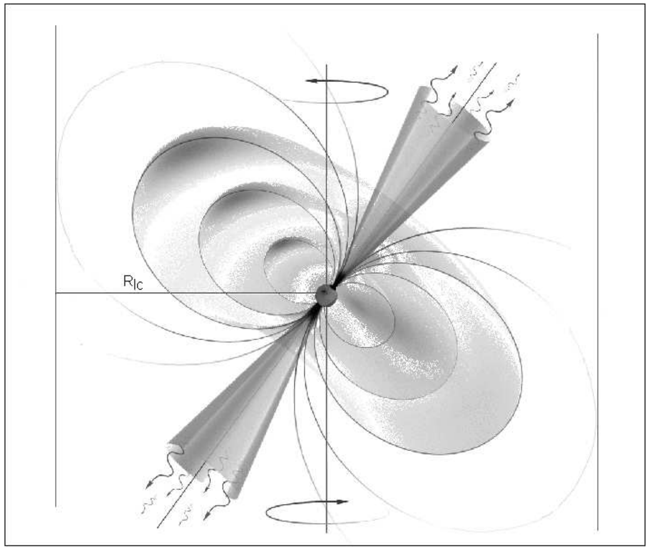

Figure 1.2: Polar-cap model for the radio pulsar emission mechanism.

One of the most commonly accepted models for the radio emission mechanism of pulsars, the so-called polar-cap model, predicts that the presence of the high magnetic fields ($B \sim 10^8 - 10^{13} G$) in a fast spinning object produces an electric field so intense that it extracts charged particles from the neutron star surface. The particles are constrained to move along the magnetic field lines co-rotating with the neutron star. The co-rotation is possible only within

Chapter 5

Summary

The Parkes High-Latitude Pulsar Survey, a large scale survey covering the region of the sky enclosed by galactic longitudes $220° < l < 260°$ and galactic latitudes $|b| < 60°$, yielded the discovery of 17 new pulsars (§3) four of which belonging to the family of the millisecond pulsars (§3.2, §3.3, §4.2). The description of the survey and of the data analysis has been presented in §2. The rate of millisecond over long period pulsars found in the scanned area is much higher than for the other large scale surveys, most of which were concentrated on the galactic plane, and confirms that the adopted observing strategy was suitable for finding the elusive fast spinning objects: at higher latitudes, in fact, the effects of the interstellar medium (§1.4.1, §1.4.2) in broadening the emitted pulses are reduced; moreover it is likely that millisecond pulsars, being old neutron stars 'recycled' by mass and angular momentum transferred by a companion star (§1.3), had more time to migrate away from their birthplaces in the disk of the Galaxy and hence display a more spread distribution in height on the galactic plane that the younger long period pulsars.

Of the four millisecond pulsars discovered three belongs to a binary system, while the forth, PSR J1038+0034 (§3.3), is likely to be a mildly recycled isolated pulsar whose former companion was a massive star that ended its life in a supernova explosion probably responsible for the disruption of the binary system. If the follow-up observations will confirm this picture, this pulsar will be the third object belonging to the small class of the so-called Disrupted Recycled Pulsars (DRPs, Lorimer et al. 2004).

Among the binary pulsars discovered in the Parkes High-Latitude Survey, two are likely to have white dwarf companions, although optical observations will help in understanding their real nature: PSR J0610−2100 has a very light

a radius R_{lc} , the light cylinder radius (see fig. 1.2) given by:

$$R_{lc} = c\frac{P}{2\pi} \tag{1.7}$$

Beyond this radius the speed of the field lines would be greater than the speed of light: the field lines must hence be open. Using the equation that describes the magnetic field lines of a dipolar field ($\sin^2\theta/r = const$) we can define the angle θ_p formed at the magnetic poles of the star by the last open field line:

$$\frac{\sin^2\theta_p}{R} = \frac{\sin^2 90\deg}{R_{lc}} \qquad \rightarrow \qquad \sin\theta_p = \sqrt{\frac{2\pi R}{cP}} \tag{1.8}$$

This angle naturally delimits a conal-like set of field lines. The particles moving along these open field lines give rise to the radio emission (probably curvature radiation) confined in a beam of semi-amplitude θ_p. Because of the misalignment of the magnetic and rotational axes, the collimated emission appears pulsating with a period equal to the spin period of the neutron star to any observer whose line of sight crosses the radio beam.

1.3 Binary and Millisecond Pulsars

When a pulsar crosses the death line the emission mechanism fails and the neutron star ceases to behave as a radio pulsator. If the neutron star belongs to a binary system, during the evolution of the companion star matter and angular momentum can be transferred via wind or more efficiently via Roche Lobe Overflow (RLO) on the neutron star. During this accretion phase the neutron star is visible as X-ray source, its period decreases (the star is spun-up by angular momentum transfer) and its magnetic field decays, probably because of the accretion itself (see e.g. Miri & Bhattacharya 1994 and Urpin, Geppert & Konekov 1998 for alternative explanations of the magnetic field decay). Depending on the mass of the companion and hence on the duration of the mass transfer phase, at the end of the accretion the spin period and magnetic field can be such that the neutron star is again above the death line, in the bottom-left part of the $P - \dot{P}$ diagram. These reborn pulsars are called millisecond pulsars (because of their short rotational periods) or *recycled* pulsars. The model described above for the formation of this class of objects is the so-called *recycling model*, developed in the early 80s by Ali Alpar and collaborators (Alpar et al. 1982).

Let's see in more detail the evolution followed by a binary system giving rise to a millisecond pulsar (fig. 1.3).

We start with a system composed of a primary star having mass $M \gtrsim 8$ $M_\odot$ and a secondary with mass $M_2 \lesssim 1$–2 $M_\odot$. The more massive star evolves becoming a red giant, filling its Roche Lobe and losing mass until only a helium core is left. The first stage of the evolution ends with the helium core implosion, the supernova explosion and the creation of a compact remnant. If the system doesn't remain gravitationally bound, the newly born neutron star evolves as an isolated pulsar as described in §1.2, otherwise we obtain a binary system containing a neutron star with a typical mass $M_{NS} \sim 1.4$ $M_\odot$ and a low mass main sequence star. At that point the neutron star can be seen as a young radio pulsar in a binary system. As long as the (possible) wind from the companion star is swept by the pulsar radiation pressure up to the light cylinder radius and/or the gravitational radius, given by:

$$R_G = \frac{2GM}{v_w^2} \tag{1.9}$$

(where v_w is the velocity of the wind from the companion), the pulsar steadily spins down following the equation 1.3 (*ejector* phase). Because of the slowing down, the pulsar wind pressure drops off and the matter carried in the companion wind reaches the magnetospheric radius R_m. This quantity, defined as a fraction $\phi \lesssim 1$ of the the Alfvèn radius, at which the magnetic field pressure $P_{mag} = B^2/8\pi$ equals the pressure of a spherically infalling matter $P_{gas} = \rho_{gas}/v_w^2$ (with ρ_{gas} the density of the gas), can be written as:

$$R_{mag} = \phi 9.8 \times 10^5 B_8^{4/7} M_{NS}^{-1/7} R_6^{10/7} \dot{M}_E^{-2/7} \qquad \mathrm{cm} \tag{1.10}$$

where B_8 is the pulsar magnetic field in units of 10^8 Gauss, M_{NS} is the mass of the neutron star in solar masses, R_6 is the radius of the neutron star in units of 10^6 cm and $\dot{M}_E$ is the mass transfer rate in Eddington units (i.e. $1.5 \times 10^{-8} R_6$ $M_\odot$ yr^{-1}, Burderi, King & Wynn 1996). At this point, if at R_{mag} the velocity of the magnetic field lines is greater than the keplerian velocity, the *propeller* phase begins in which the centrifugal force exerted by the magnetosphere expels the infalling matter from the system. In this phase the neutron star loses angular momentum and the pulsar spins down. When the velocity of the magnetic field lines at the magnetospheric radius becomes smaller than the keplerian velocity, the centrifugal barrier is open and the

the light cylinder radius of B, the energy density of the relativistic wind from A is about two orders of magnitude greater than that from B, ensuring that the wind from A is penetrating deep into B's magnetosphere. Assuming isotropy, one find that the energy densities due to the spin-down luminosity emitted by A and the magnetic field of B are in balance at a distance $\sim$0.2 lt-s from B, about 40% of its light cylinder radius. These calculations are valid in the assumption that the magnetic field of pulsar B can still be computed using the standard dipole formula given in §1.2, although exposed to A's emission. Even though this picture is roughly consistent with the lateral extent of the observed eclipse of A, it is likely that the strong departure of B's magnetosphere from an ideal case makes such calculations uncertain.

In any case, because the point of pressure-balance is deep within the magnetosphere of B, the actual penetration of the wind from A into B's magnetosphere is likely to be a function of the orientation of the rotation and/or magnetic axes of B relative to the direction of the wind and hence it will depend on the precessional and orbital phases of B. This is the most likely explanation for the large flux density and pulse-shape changes of B which are seen to vary with orbital phase (fig. 4.7 and 4.8). As pointed out in §4.2.2 these changes are essentially the same between 680 MHz and 3030 MHz. It seems most likely that such a broadband modulation arises from the impact of energy in the form of particles, gamma-rays or 44-Hz electromagnetic radiation from the millisecond pulsar A upon the magnetosphere of B. The front shock produced in such a violent interaction is probably also the cause of the short eclipse in pulsar A's emission and of the $\sim$5 mJy unpulsed emission observed at 1.4 GHz.

In summary, the close interactions between the two pulsars is for the first time giving the possibility to have a better understanding of pulsars' magnetospheres and emission processes and issues many interesting observational and theoretical challenges: monitoring the changes in the pulse shapes and the flux and polarisation variations along the orbit at many different frequencies will be very important in the aim of assessing the nature of the puzzling behavior of PSR J0737−3039A and PSR J0737−3039B and for better exploiting the J0737−3039 system as a test bed for relativistic gravity.

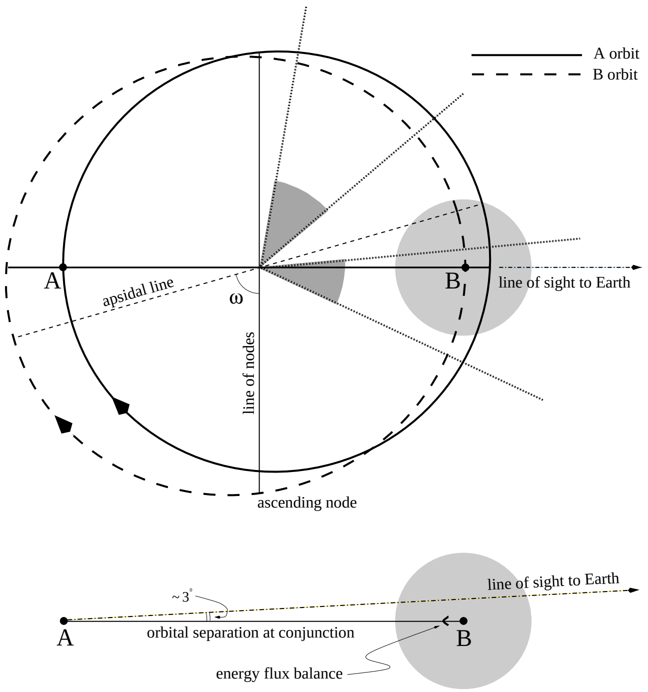

Figure 4.13: The physical configuration of the binary system, at conjunction, as on 19 August 2003 (MJD 52870), showing the relative sizes of the two orbits and B's magnetosphere. Top: view from above the orbital plane with the Earth to the right. The shaded segments indicate orbital phases where B is detected strongly (see fig. 4.7). Bottom: view from the side, showing the passage of the line-of-sight from A to the Earth through the magnetosphere of B. The approximate position of the pressure balance between the relativistic wind from A and the magnetic field of B is indicated.

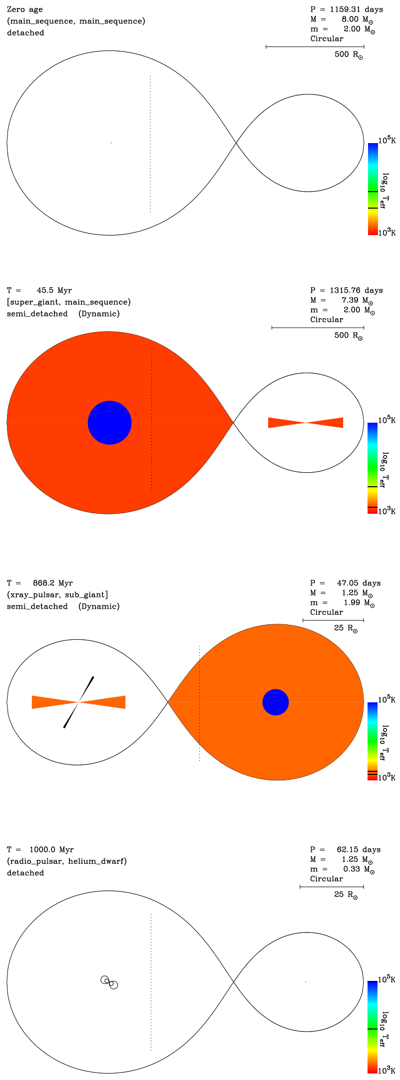

Figure 1.3: Evolutionary path for a binary system containing a 9.0 $M_{\odot}$ and a 2.0 $M_{\odot}$ stars (from `http://www.manybody.org/cgi-bin/starlab/binary_demo.pl`). From top to bottom: main sequence - main sequence; first Roche Lobe overflow (followed by a supernova explosion that leaves a NS); second RLO (the NS shines as X-ray source); end of the mass transfer on the NS: the NS shines as radio pulsar and secondary star is a WD.

matter carried by the wind of the companion star starts to be accreted on the neutron star surface. At this point the neutron star's spin period slowly decreases. The key phase for the recycling model is the final phase, when the companion star fills its Roche Lobe and starts to transfer matter onto the neutron star surface at much higher rates than before (up to 10^{-8} $M_{\odot}$/yr). For an accretion rate $\dot{M}_{acc}$, the matter transferred can spin-up the neutron star to a minimum period $P_{min} \propto B^{6/7}\dot{M}_{acc}^{-3/7}$ at which the rotational velocity equals the keplerian velocity of the inner rim of the accretion disk: the accretion of angular momentum stops and the neutron star is placed on the $P-\dot{P}$ diagram on the so-called spin-up line (in fig. 1.1 traced for $\dot{M}_{acc} = \dot{M}_E$). In low mass binary systems, as the one described here, the RLO phase (or *accretor* phase) lasts $10^7 - 5 \times 10^8$ yr at the end of which the neutron star reaches periods of few milliseconds and magnetic fields in the range $10^8 - 10^9$ G. When the stellar surroundings are free of matter (at least up to the light cylinder radius), the neutron star, being above the death line, starts shining again as radio pulsar.

1.4 Basic Observational Properties

Following what discussed in §1.2 and §1.3, pulsars can be subdivided in two families: the long period pulsars, with periods ranging from $\sim$ 0.1 to 8 seconds and magnetic fields $B \sim 10^{11} - 10^{13}$ G, and the millisecond (or recycled) pulsars, with periods $P \lesssim 50$ ms and magnetic fields in the range $10^8 - 10^9$ G.

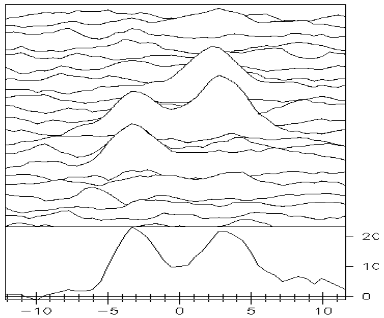

Figure 1.4: Single pulses (top) and averaged profile (bottom) for PSR B0834+06.

be as high as 1 every 1-2 years at 95% confidence level. It is the first time that the estimated double neutron star detection rate enters within astrophysically relevant regimes.

After a few years of operation of the gravity wave detectors, it should be possible to test these predictions directly and thus place better constraints on the cosmic population of double neutron star binaries.

4.3.3 Probing the Pulsars' Magnetospheres

The separation of the two pulsars in their orbits (as schematically represented in the top part of figure 4.13) is typically $\sim$900,000 km (or 3 lt-s). The large orbital inclination deduced from the measurement of the shape of the Shapiro delay, $s \equiv \sin i$, or from the comparison of the constraints given in the mass-mass diagram by the measured mass ratio, R, and periastron advance, $\dot{\omega}$ (see table 4.3), implies that, at conjunction, the line-of-sight to one pulsar passes within about 0.15 lt-s of the other (fig. 4.13, bottom). This is substantially smaller than the 0.45 lt-s radius of J0737−3039B's light cylinder (eq. 1.7), although much greater than the 0.004 lt-s light cylinder radius of pulsar A. As the pulsars move in their orbits, the line-of-sight from A passes through, and sweeps across, the magnetosphere of B, providing the opportunity to probe its physical conditions. The determination of changes in the radio transmission properties, including the dispersion and rotation measures, will potentially allow the plasma density and magnetic field structure to be probed. Additionally, the $\sim$70-yr period geodetic precession will cause the line-of-sight to sample different trajectories through the magnetosphere of pulsar B.

As described in §4.2.2 close inspection of the flux density of the pulses from PSR J0737−3039A (fig. 4.6) reveals that a short occultation occurs, centered upon its superior conjunction (when the line-of-sight passes only 0.15 lt-s from pulsar B). The duration of the occultation is about 20–30 sec. Because the relative transverse velocity is about 660 km/s, the eclipsing region has a lateral extent of $\sim$15,000 km or $\sim$0.05 lt-s, about 10% of the light cylinder radius of B. From the data obtained so far it appears that the eclipse occurs in every orbit and its extent is essentially the same at 680 MHz, 1390 MHz and 3030 MHz, limiting the possible interpretations of the processes that are causing it. One clue may come from the fact that the rate of spin-down energy loss from pulsar A is $\sim$3000 times greater than that from B (see table 4.3). In fact, at

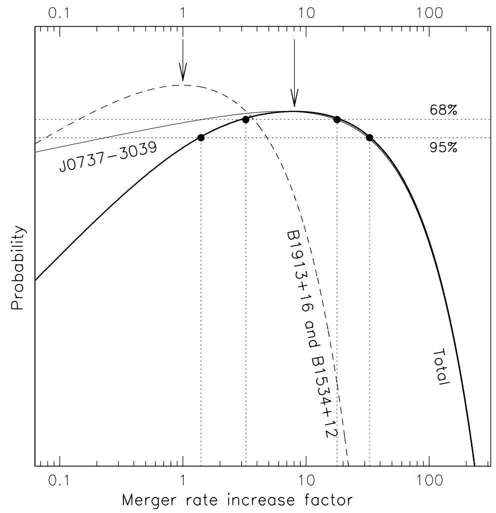

Figure 4.12: Probability density function for the increase in the double neutron star merger rate $(\mathcal{R}_{0737} + \mathcal{R}_{1913} + \mathcal{R}_{1534})/(\mathcal{R}_{1913} + \mathcal{R}_{1534})$ resulting from the discovery of J0737−3039 system. The dashed curve represents the reference probability density function corresponding to the merger rate calculated on the basis of PSR B1913+16 and B1534+12 only, the thick solid curve is the new probability density function accounting also for J0737−3039 system. The dotted vertical lines delimits the 68% and 95% confidence levels on the determination of the increase factor. The dominant role of J0737−3039 system in shaping the new statistics of DNS coalescence rate is evident (solid thin curve).

and PSR B1913+16 are different, using another reference frequency would give different scaling factors: in particular, comparing the luminosity of PSR J0737−3039A and B1913+16 at 1400 MHz instead of using the reference 400 MHz frequency, would further increase the luminosity ratio and the total scaling factor.

In summary, the discovery of J0737−3039 system sets a firm lower limit to the merger rate increase factor of about six. The actual predicted value of the Galactic merger rate, and hence the detection rate by gravity wave detectors, depends on the shape of the pulsar luminosity function. For the most favorable distribution model available, the updated cosmic detection rate for first-generation gravity wave detectors such as VIRGO, LIGO and GEO can

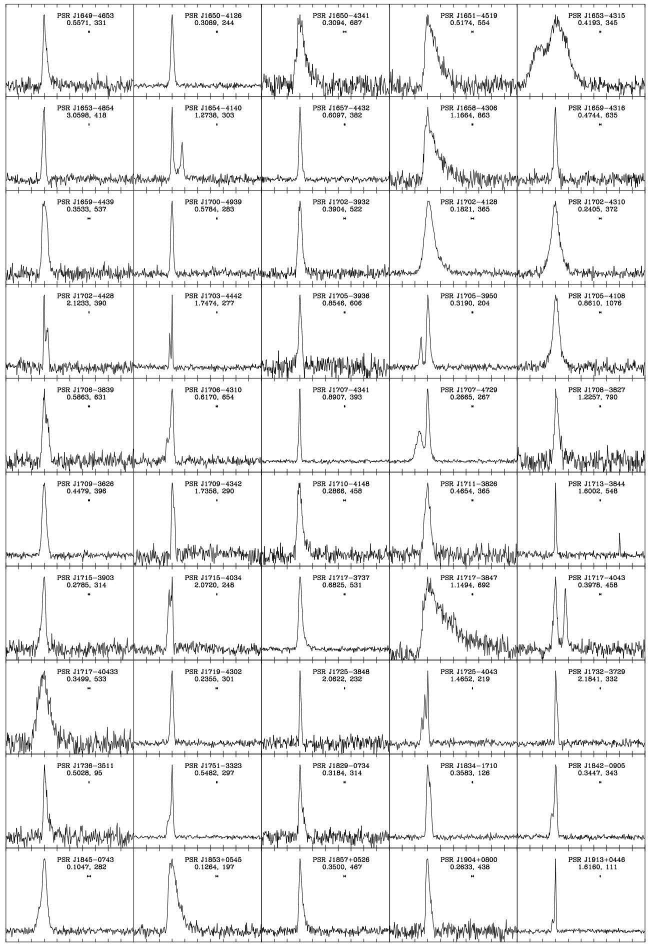

Figure 1.5: Examples of integrated pulse profiles for different pulsars (Kramer et al. 2003).

Duty cycles (i.e. the duration of the pulse over the period) are typically $1-5\%$ for long period pulsars and from $\sim 5\%$ up to $\gtrsim 30\%$ for millisecond pulsars (Kramer et al. 1998). Pulse shapes are highly variable from pulse to pulse (fig. 1.4) but the integrated profile (averaged over few hundreds of cycles) is extremely stable and represents a sort of "fingerprint" for a pulsar (fig. 1.5).

The observed pulse shapes, because of the interaction between the broad band radio signal and the interstellar medium (ISM), usually appear different from the emitted pulses. The principal effects of the ISM on the radio emission are the dispersion and the scattering of the pulsed signal both producing a broadening of the pulse profile.

1.4.1 Dispersion

The dispersion of a broad band pulsed signal is due to the fact that the group velocity v_g of an electromagnetic wave in a plasma depends on the emission frequency ν of the signal. This quantity can be written as.

$$v_g = c\sqrt{1-\left(\frac{\nu_p}{\nu}\right)^2} \tag{1.11}$$

where the term under square root represents the refractive index of the medium and $\nu_p = \sqrt{e^2 n_e/\pi m_e}$ (with e, n_e and m_e, the charge, the number density and the mass of the electron respectively) is the plasma frequency, below which a signal is totally absorbed. For a frequency $\nu \gg \nu_p$ we can write the group velocity as:

$$v_g = c\left[1-\frac{1}{2}\left(\frac{\nu_p}{\nu}\right)^2\right] \tag{1.12}$$

The time taken by a signal with a frequency ν to reach the observer is then given by:

$$t = \int_0^d \frac{dl}{v_g} \sim \int_0^d \frac{1}{c}\left[1+\frac{1}{2}\left(\frac{\nu_p}{\nu}\right)^2\right] dl = \frac{d}{c} + \frac{1}{2}\frac{e^2}{\pi m_e c}\frac{1}{\nu^2} DM \tag{1.13}$$

where $DM = \int_0^d n_e dl$ is the *dispersion measure* and d is the distance to the observer. Since the radio pulsar signal is broad band, the dependence of t on the frequency produces a broadening Δt_{DM} of the pulse profile:

$$\Delta t_{DM} = \frac{e^2}{2\pi m_e c}\left(\frac{1}{\nu_1^2}-\frac{1}{\nu_2^2}\right) DM \sim 8.3\cdot 10^3 \frac{\Delta\nu_{MHz}}{\nu_{MHz}^3} DM \quad \mathrm{s} \tag{1.14}$$

the following. Under this assumption, the pulsed luminosity at 400 MHz for PSR J0737−3039A results $L_{0737} \sim 30$ mJy kpc^2, much lower than that of PSR B1913+16 (~ 200 mJy kpc^2).

For a planar homogeneous distribution of pulsars in the Galaxy, the ratio N_{0737}/N_{1913} scales as $L_{1913}/L_{0737} \sim 6$. Therefore we obtain $\mathcal{R}_{0737}/\mathcal{R}_{1913} \sim 12$. Including the moderate contribution of the longer-lived PSR B1534+12 system to the total rate (van den Heuvel & Lorimer 1996, Arzoumanian, Cordes & Wasserman 1999, Kalogera et al. 2001, Kim, Kalogera & Lorimer 2003), we obtain an increase factor for the total merger rate $(\mathcal{R}_{0737}+\mathcal{R}_{1913}+\mathcal{R}_{1534})/(\mathcal{R}_{1913}+\mathcal{R}_{1534})$ of about an order of magnitude. A better estimate of this factor and its uncertainty can be obtained using a bayesian statistical approach (Kim, Kalogera & Lorimer 2003).

Figure 4.12 displays such an estimate, reporting the probability density function for the merger rate increase factor. It shows a peak value of ~ 8 and an upper limit of ~ 30 at a 95% confidence level. For a given class k of binary pulsars, the probability density function $P(\mathcal{R}_{\rm k})$ for the corresponding merger rate $\mathcal{R}_{\rm k}$ is obtained from the relation $P(\mathcal{R}_{\rm k}) = A^2\mathcal{R}_{\rm k}e^{-A\mathcal{R}_{\rm k}}$ where $A = \tau_{\rm k}/(N_{\rm k}f_{\rm k})$ and $f_{\rm k}$ is the correction factor due to the beamed nature of the radio pulsar emission (Kim, Kalogera & Lorimer 2003). The beaming factor for PSR J0737−3039A is chosen as the average of the beaming factors of the two other coalescing DNSs.

The conservative result obtained here, in the simple assumption of a fixed pulsar luminosity and a uniform disk distribution of pulsar binaries, can be refined by including the parameters of the Parkes High-Latitude Pulsar Survey into a simulation programme modelling survey selection effects (and hence detection probability) and the Galactic population of pulsars. Extensive simulations (Kalogera et al. 2004) produce results consistent with that derived in fig. 4.12 and show that the peak of the merger rate increase factor resulting from the discovery of J0737−3039 system lies in the range 6 to 7 and is largely independent of the adopted pulsar population model.

It is important to point out that the numbers obtained here are lower limits on the scaling factor: if the real distance of the double pulsar system is lower than the assumed value of 1 kpc, the luminosity of PSR J0737−3039A would be smaller and the scaling factor on the number of sources could easily double. Note, moreover that, since the spectral indices of PSR J0737−3039A

uncertainty of about 50% from the dispersion measure, ~ 1 kpc from X-ray absorption) is an order of magnitude less than that of PSR B1913+16. These properties have a substantial effect on the prediction of the rate of merging events in the Galaxy.

For a given class k of binary pulsars in the Galaxy, in fact, apart from a beaming correction factor, the merger rate $\mathcal{R}_{\rm k}$ is calculated (Kim, Kalogera & Lorimer 2003) as $\mathcal{R}_{\rm k} \propto N_{\rm k}/\tau_{\rm k}$. Here $\tau_{\rm k}$ is the binary pulsar lifetime defined as the sum of the time since birth, $\tau_{\rm b}$, and the remaining time before coalescence, $\tau_{\rm m}$ whereas $N_{\rm k}$ is the scaling factor defined as the number of binaries in the Galaxy belonging to the given class. The value of τ_b for PSR J0737−3039A can be computed as the time since the pulsar left the spin-up line (as calculated by Arzoumanian, Cordes & Wasserman, 1999) and it results $\sim$ 150 Myr. Alternatively one can assume that the characteristic age of pulsar B is a reliable estimate of the true age of both pulsars. In this case $\tau_b \sim 50$ Myr. In either cases the life time of PSR J0737−3039 is much shorter than that of PSR B1913+16 (τ_{1913}/τ_{0737} = (365 Myr)/(235 − 135 Myr) $\sim 1.6 - 2.7$, where the subscript numbers refer to the pulsars), implies roughly a doubling of the ratio $\mathcal{R}_{0737}/\mathcal{R}_{1913}$. A much more substantial increase results from the computation of the ratio of the scaling factors N_{0737}/N_{1913}.

Since the available numbers for the coalescence rate of double neutron star systems in the Galaxy, to which the computed scaling factors apply, are derived using a population synthesis code whose parameters are based mostly on the results of surveys done at 400 MHz (van den Heuvel & Lorimer 1996, Arzoumanian, Cordes & Wasserman 1999, Kalogera et al. 2001, Kim, Kalogera & Lorimer 2003), we adopt here 400 MHz as reference frequency for comparing the luminosity of the two pulsars in question.

The flux at 400 MHz for PSR J0737−3039A has been computed scaling the pulsed flux measured at 1.4 GHz using a spectral index $SI \sim 2.3$ obtained from observations at 10, 20, 50 and 70 cm with the Parkes radio telescope. To calculate the luminosity it's then necessary to assume a distance for the pulsar. Since, as mentioned in §4.2.3, the DM derived distance, ~ 0.6 kpc, is uncertain by a factor of two or more in the region of the sky where J0737−3039 system is located and since the equivalent hydrogen column density value derived from the X-ray observations suggest a distance ~ 1 kpc, to be conservative on the assessment of the scaling factors, we will adopt the latter value in

where ν_{MHz} and $\Delta\nu_{MHz}$ are the central observing frequency and the total bandwidth in MHz respectively and DM is given in pc cm^{-3}.

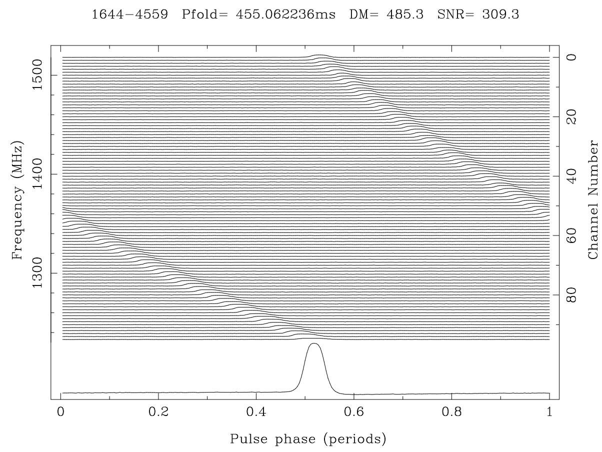

Figure 1.6: Effect of the dispersion on the pulse of PSR J1644-4559. In this observation we used a total bandwidth $\Delta\nu$ = 288 MHz, split into 96 × 3 MHz channels, and a central frequency ν = 1372.5 MHz. The bottom integrated profile is obtained by dedispersing the signal (see text).

One method for minimizing the effects of the dispersion is to split the total bandwidth into several channels having a frequency width $\delta\nu$. In this way, in each frequency channel, the pulse is poorly affected by the dispersion in the ISM and the signal in the different channels appears as in figure 1.6, with the pulses arriving in each channel at a different time. Knowing the dispersion measure allows to correct for this time shift integrating the signal along the line connecting the edges of the pulses in each channel (*dedispersion* of the signal) and obtaining a sharp and high signal-to-noise profile.

Better results can be obtained applying the so-called *coherent de-dispersion* method, in which the incoming signals are de-dispersed over the whole bandwidth using a filter which has the inverse transfer function to that of the interstellar medium (Hankins & Rickett 1975). As a result, the pulse profile is perfectly aligned in frequency, without any residual dispersive smearing caused by finite channel bandwidths (fig. 1.7). The maximum time resolution obtainable via coherent de-dispersion is the inverse of the receiver

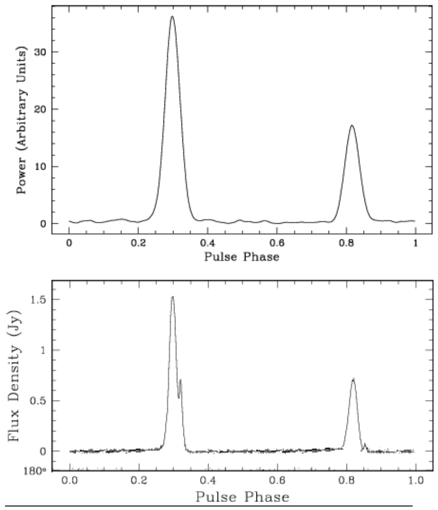

Figure 1.7: Profiles of PSR B1937+21 obtained with filterbanks (top) and using coherent dedispersion (bottom).

bandwidth: for a 288 MHz bandwidth, such that used for the observations presented in this work, this technique makes it possible to resolve features on time-scales as short as few nanoseconds.

1.4.2 Interstellar Scattering

The inhomogeneities in the ISM act like center of scattering onto the signal emitted from a pulsar. Because of this interaction with clumps of matter, the radio waves follow different paths and arrive at the observer at different times (fig 1.8) thus producing a broadening δt_{scatt} of the pulse. According to the simple "thin screen" model δt_{scatt} scales as:

$$\delta t_{scatt} \propto \frac{DM^2}{\nu^4} \tag{1.15}$$

Unlike the case of the dispersion, no technical skills can be adopted to mitigate the effects of interstellar scattering. The only way to reduce its effect is to observe at higher frequencies.

Using a high frequency reduces the broadening of the pulses caused by the interaction of the radio signal with the interstellar medium (both dispersion

through it should rapidly changing. On the other hand geodetic precession may also have the undesirable effect of making the pulsar undetectable in a short time (PSR B1913+16, because of this, is expected to disappear in 2025; Kramer 1998)

In the next few years, several more relativistic effects are expected to be measured, some dependent on higher-order terms in the post-Newtonian expansion (i.e. $\ddot{\omega}$). These will provide the tightest constraints yet on theories of gravity in the strong-field regime.

4.3.2 Gravitational Waves Detection

Because of emission of gravitational waves, double neutron star systems lose orbital energy (Taylor & Weisberg 1989). As a consequence the two stars undergo an orbital spiral-in at the end of which they merge producing a burst of gravitational waves.

Coalescence of DNS are one of the prime target for ground based gravitational wave detectors such as LIGO (Abramovici et al. 1992), GEO (Danzmann et al. 1995) and VIRGO (Caron et al. 1997) and the expected rate of these events is clearly an important factor for the development of these instruments (Thorne & Cuttler 2002).

Of the five double neutron star system known (Taylor 1992) before the discovery of PSR J0737−3039 system, only three have orbits tight enough that the two neutron stars will coalesce within a Hubble time. Two of them (PSR B1913+16 and PSR B1534+12) are located in the galactic field, while the third (PSR B2127+11C) is found on the outskirts of a globular cluster. The contribution to the galactic DNS coalescence rate $\mathcal{R}$ of globular cluster's pulsars is estimated to be negligible (Phinney 1991); also, recent studies (Kim, Kalogera & Lorimer 2003) have demonstrated that the current estimate of $\mathcal{R}$ relies mostly on PSR B1913+16. Hence, a rough assessment of the contribution of the discovery of J0737−3039 system to the estimates of double neutron star merger rate can be done by comparing its properties with those of PSR B1913+16.

PSR J0737−3039A and B will coalesce due to the emission of gravitational waves in a merger time $\tau_{\mathrm{m}} \sim 85$ Myr, a timescale that is a factor 3.5 shorter than that for PSR B1913+16 (Taylor, Fowler & McCulloch 1979). In addition, the estimated distance for J0737−3039 system ($\sim$ 600 pc with an intrinsic

region permitted by the measured values of the range r and shape s of the Shapiro delay. The inset in figure 4.11 is an enlarged view of the small square which encompasses the intersection of the three tightest constraints (with the scales increased by a factor of 16). Note that all the plotted curves derived from the General Relativity equations 4.1 to 4.5, intersects each other on the mass ratio R line.

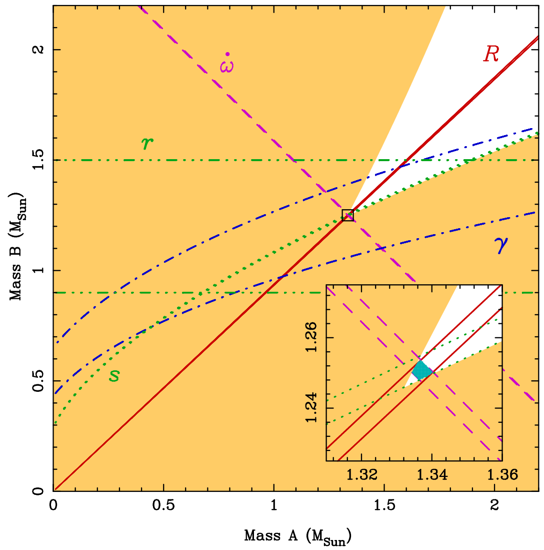

Figure 4.11: The observational constraints upon masses M_A and M_B. For an explanation of the different curves see text.

Another important and extreme characteristic of PSR J0737−3039A and B is the predicted geodetic spin-precession due to curvature in space-time around the pulsars: according to Einstein's theory, if the rotational and orbital angular momenta are misaligned, the spin axis of pulsar A should be moving around the axis perpendicular to the orbital plane at a rate of 4.79 °/yr, four time larger that the largest measured to date (1.2 °/yr for B1913+16). This implies a period for the geodetic precession of only 75 years for pulsar A. The same calculations applied to pulsar B give a geodetic precession period of 71 yr. This property should allow detailed mapping of the pulsar emission beam (Weisberg & Taylor 2002) in few years, since the observer's line of sight

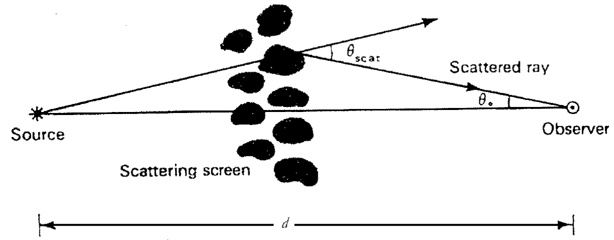

Figure 1.8: Effect of the interstellar scattering on the photons emitted by a celestial source.

and scattering) and also reduces the sky background noise ($\propto \nu^{-2.7}$). On the other hand the typical pulsar spectrum at radio wavelength is a steep power-law $S(\nu) \propto \nu^{-\alpha}$ with spectral index $\alpha \sim 1.6$. The choice of the observing frequency, hence, is a crucial point in any observational campaign.

$\sim$ 30 years (Taylor & Weisberg 1989, Weisberg & Taylor 2003), and all five PK parameters in $\sim$ 10 years (Stairs et al. 2002) respectively. This comparison gives an idea of the possibilities that J0737−3039 system opens in this field. It is worth noting, for instance, that using only the information given by pulsar A and in less than a year of follow-up observations, J0737−3039 system already tests General Relativity with very high accuracy: the measured value of the shape of the Shapiro delay, s_{obs}, agrees with Einstein's predictions, s_{GR}, at about 0.3% level:

$$\frac{s_{obs}}{s_{GR}} = 1.0007(22) \tag{4.6}$$

This can be compared with the 0.2% agreement resulting from the measurement of the orbital decay in PSR B1913+16 (Weisberg & Taylor 2003), although the two tests belong to different classes, since the latter checks the radiative predictions of General Relativity, whereas the former involves only non-radiative timing parameters.

Having detected the pulsations also from the second neutron star in the binary system allows for the first time to perform even better and significant tests of relativistic gravity: the timing measurement of the projected semi-major axis of both pulsars, in fact, yields the measurement of the mass ratio R of the two neutron stars. This value gives a qualitatively different constraint to the masses of the stars, since the relation

$$R \equiv \frac{a_B}{a_A} = \frac{M_A}{M_B} \tag{4.7}$$

is largely independent on the adopted theory of gravity. In fact, equation 4.7 is valid for all 'fully conservative' theories as defined by Will (1992) and in particular for all Lagrangian-based theories (Damour & Taylor 1992). Hence, for any given set of equations describing the post-keplerian parameters, the lines formed on the mass-mass diagram must cross on the line indicating the mass ratio.

In figure 4.11 all the constraints on the masses of PSR J0737−3039A and PSR J0737−3039B are plotted: the coloured regions of the diagram is ruled out by A and B's mass functions, red lines enclose the region permitted by the calculated range for the mass ratio, dashed purple curves indicate the constraint imposed by the advance of periastron measurement, blue dot-dashed lines are from the measured gravitational redshift – time dilatation parameter γ, green triple dot-dashed lines and dotted curves enclose respectively the

luminosity results $L_X \sim 2 \times 10^{30}$ erg/s. It is important to point out that the DM derived distance, especially in this region of the sky near the Gum Nebula may be uncertain by a factor of two or more (Mitra & Ramachandran 2001). The derived luminosity is hence uncertain by at least a factor of four.

Whether resulting from magnetosphereic or thermal processes, most pulsars emit of the order of $10^{-3} \times \dot{E}$ in soft X-rays (Becker & Trümper 1999). While PSR J0737−3039B is not expected to have a detectable X-ray flux, pulsar A's magnetosphere could be solely responsible for all the observed luminosity, although the spectral index found in the fit is a bit steep compared to the usual value observed in the sample of rotation powered pulsars emitting in the X-ray band ($\Gamma \sim 2 - 2.4$). Anyway, uncertainties in spectral parameters and in the distance assumed leave open many possible interpretations and deeper observations are required in order to better investigate the X-ray emission properties along the orbit of J0737−3039 system.

In §4.3.3 possible interpretations of what's causing A's eclipses and B's flux and profile changes along the orbit and what's responsible for the radio unpulsed emission (and maybe partially for the X-ray emission) observed, are presented.

4.3 Implications

4.3.1 Testing Relativistic Gravity

Since the only unknowns in the left hand side of equations 4.1 to 4.5 (or their analogues in other relativistic gravity theories) are the masses of the two stars in the binary system, the measurement of two post-keplerian parameters yields the masses and the measurement of three or more PK-parameters over-determines the system. In other words, once the masses are obtained measuring any two PKs, their value can be placed in the equation of 3rd, 4th and 5th parameter and the values obtained can be compared with the measured ones, giving a self-consistency test of the theory on which the given equations are based.

Timing of PSR J0737−3039A over $\sim$ 10 months led to the measurement of 4 post-keplerian parameters (see tab. 4.1). For the two other pulsars belonging to a double neutron star system on which these kind of measurements have been successfully done, B1913+16 (Hulse & Taylor 1975) and B1534+12 (Wolszczan 1991), timing observations yielded the measurement of three PK parameters in

Chapter 2

The Parkes High-Latitude Pulsar Survey: Observations and Data Reduction

2.1 Observations

The Parkes High-Latitude (PH) Pulsar Survey covers the region enclosed by Galactic longitude $220° < l < 260°$ and Galactic latitude $|b| < 60°$ for a total of 6456 pointings of 265 s duration each. The observations, started in November 2000 and completed in December 2003, were made using the multibeam receiver (Staveley-Smith et al. 1996) on the Parkes 64-m radio telescope (NSW, Australia) operating at a central frequency of 1347 MHz and consisting of 13 separate beams (fig. 2.1). The total 288 MHz bandwidth was subdivided into 2×96 3 MHz channels in order to minimise the pulse broadening due to dispersion in the interstellar medium (see §1.4.1). The signal was one-bit sampled every 125 μs and recorded on Digital Linear Tapes for off-line analysis.

The 13 beams of the multibeam receiver are spaced by approximately two beamwidths in the sky so that a given area is entirely covered by four pointings placed as shown in the right panel of fig. 2.1. This cluster of pointings covers a region about 1.5° across, with adjacent beams overlapping at the half power points. An interactive programme, `hexaview` is used to display the status of each pointing ("selected", "observed" or "processed", see fig. 2.2) and to select pointings for observation.

The minimum detectable flux density for a pulsar of period P can be described by the following equation (e.g. Manchester et al. 1996):

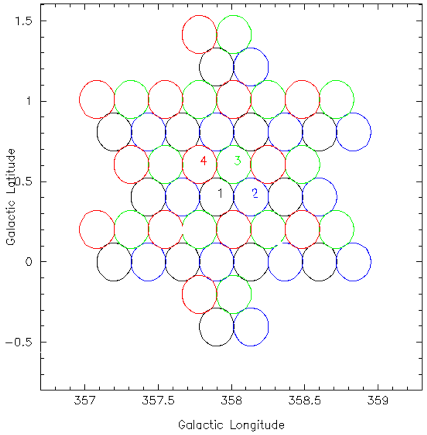

Figure 2.1: Left panel: the Multibeam receiver. Right panel: beams locations for a cluster of four pointings.

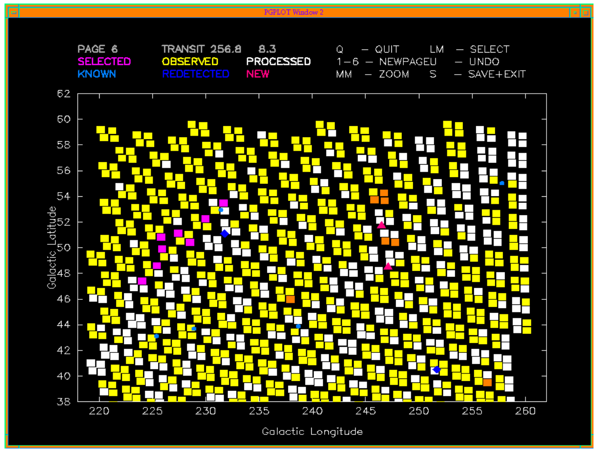

Figure 2.2: Output plot for `hexaview`: yellow squares are observed pointings, orange ones are not observed, magenta ones are selected and white ones are the pointings already processed.

In January 2004 a DDT (Director Discretionary Time) proposal has been accepted for an X-ray observation of the PSR J0737$-$3039 system with *Chandra* X-ray Observatory. The pulsar was observed with the Advanced CCD Imaging Spectrometer S-Array (ACIS) for 10 ks. As shown in figure 4.9, a source at RAJ $= 07^h37^m51.23^s$, DECJ $= -30°39'40.9''$ has been detected and no other source is present in the ACIS S3 chip (McLaughlin et al. 2004). The position is $0.3''$ away from that derived from radio observations, well within the X-ray 1-σ position uncertainty of $0.8''$. McLaughlin et al. (2004) determined that 77 ± 9 counts originate from the J0737$-$3039 system, corresponding to a rate of $(7.7 \pm 0.9) \times 10^{-3}$ counts/s. The system is detected as a point source, with the spatial spread consistent with the point spread function of the instrument.

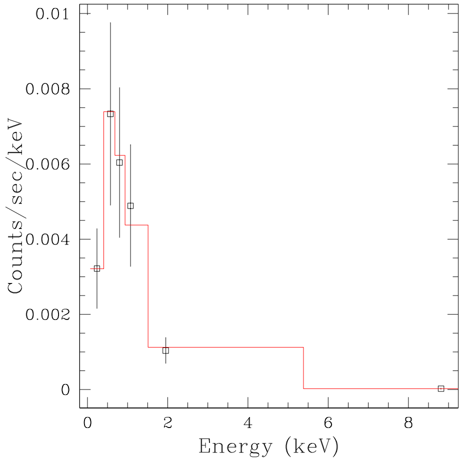

Figure 4.10: Background-subtracted spectrum of PSR J0737$-$3039 (squares), with the power law fit described in the text (solid line). The error bars account for uncertainties in both source counts and the instrumental model (McLaughlin et al. 2004).

As shown in figure 4.10, a steep power-law spectrum with spectral index $\Gamma \sim 2.9$ and equivalent hydrogen column density $N_H \sim 5 \times 10^{20}$ cm^{-2} fits the data satisfactorily (McLaughlin et al. 2004). The derived count rate and spectral fit give a 0.2–10 keV unabsorbed flux $f_X \sim 8 \times 10^{-14}$ erg cm^{-2} s^{-1}. Assuming isotropic emission and for a distance $d \sim 0.6$ kpc the 0.2–10 keV

Figure 4.8 shows the mean profiles of B around orbital phase 210° (left panel), where it appears as a narrow intense main pulse with a week precursor, phase 280° (central panel), where it becomes a roughly equal double component profile and phase 0° (right panel), where it is essentially a single pulse. As explained in 1.4, pulsar's profiles, once integrated over a reasonable number of periods, are extremely stable: B's strange behavior is unique so far and is likely due to the relativistic wind from the A pulsar penetrating deep into its magnetosphere, as will be investigated in §4.3.3.

4.2.3 Continuum Emission

Another piece of this complex picture comes from the comparison between the time-averaged pulsed flux density of pulsar A at 1390 MHz obtained from Parkes and Jodrell Bank timing observations, that results ~ 1.9 mJy, and the total flux density measured with the ATCA, ~ 7 mJy. Note that, averaged on an entire orbit, the flux contribution of pulsar B is negligible, hence we are dealing with ~ 5 mJy of unpulsed radio signal, a very strange and, again, so far unique characteristic in radio pulsars' emission properties. To better understand the nature of the observed continuum flux, a follow-up campaign at different wavelengths has been planned.

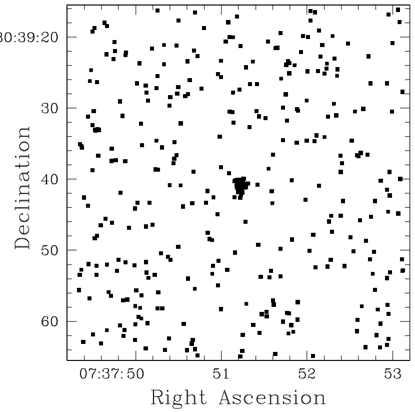

Figure 4.9: A $50'' \times 50''$ portion of the ACIS-S3 chip in the 0.2–10 keV band with the double pulsar J0737−3039 in the center. No other sources were detected in the entire $16' \times 16'$ area covered by the chip (McLaughlin et al. 2004).

$$S_{min} = \alpha \times \epsilon n_\sigma \frac{T_{sys} + T_{sky}}{G\sqrt{N_p \Delta t \Delta\nu_{MHz}}} \sqrt{\frac{W_e}{P - W_e}} \quad \text{mJy} \qquad (2.1)$$

where n_σ is the minimum signal-to-noise ratio S/N considered (here 8.0), T_{sys} and T_{sky} the system noise temperature and the sky temperature in K respectively, G the gain of the radio telescope (in K/Jy), Δt the integration time in seconds, N_p the number of polarizations and $\Delta\nu_{MHz}$ the bandwidth in MHz. ϵ is a factor ~ 1.5 accounting for sensitivity reduction due to digitization and other losses. α is a normalization factor ~ 2 that takes into account the difference between the reported equation 2.1 and the more precise limit sensitivity formula obtained by Manchester et al. (2001). This factor has been calculated here in such a way to obtain the reported sensitivity limit (0.14 mJy) for the center of the central beam of the Parkes Multibeam survey (Manchester et. al 2001). Finally, W_e is the effective width of the pulse:

$$W_e = \sqrt{W^2 + \delta t^2 + \delta t_{DM}^2 + \delta t_{scatt}^2} \qquad (2.2)$$

its value depends on the intrinsic pulse width W, on the time resolution δt of the detection apparatus and on the broadening of the pulse introduced both by the dispersion of the signal in each channel (δt_{DM}) and by the scattering induced by inhomogeneities in the ISM (δt_{scatt}).

Number of Beams	13		
Polarizations/Beam	2		
Frequency Channels	96 × 3 MHz		
System Temperature (K)	23		
Beam	Central	Inner Rim	Outer Rim
Telescope Gain (K/Jy)	0.735	0.690	0.581
Half Power Beamwidth (arcmin)	14.0	14.1	14.5

Table 2.1: Feed and receiver parameters.

Given the parameters of the multibeam receiver (see table 2.1) and the other survey parameters listed above we obtain, depending on the pulsar period and dispersion measure DM, a sensitivity limit typically in the range $0.43 - 1$ mJy.

Figure 2.3 shows the sensitivity limit as a function of P for a range of dispersion measures and for the center of the central beam of the multibeam receiver. The contribution of the sky temperature, low at high galactic latitudes, is neglected.

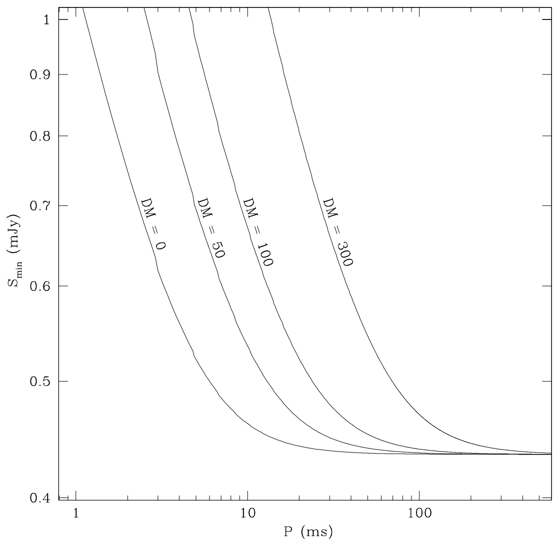

Figure 2.3: Flux limits for the PH survey as a function of the pulsar period P and for different values of DM. The plotted curves refer to the center of the central beam of the multibeam receiver and do not take into account the (negligible) contribution of the sky temperature. The value adopted here for the pulse width W is 5% of the spin period.

Using an average value of the telescope gain in the different beams, the survey sensitivity limit becomes ~ 0.49 mJy. A further degrading factor must be added (Manchester et al 2001), taking into account the non uniform beam response at the position of the pulsar relatively to the beam center (at which the values reported in table 2.1 refers). Assuming a gaussian beam shape of width 14.4 arcminutes (Hobbs et al. 2004), we end with an average flux limit for the High-Latitude survey of about 0.68 mJy.

2.2 Data Analysis

For off-line processing we used a network of eight alpha workstations at the Bologna Astronomical Observatory and, more recently, a Linux supercluster consisting of 200 CPUs at the Jodrell Bank Observatory (Manchester, UK).

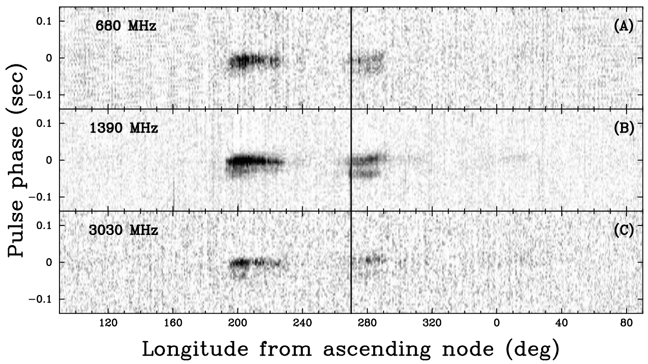

Figure 4.7: The intensity of radiation of B as a function of orbital longitude relative to the ascending node of its orbit. Each panel shows a grey-plot of intensity over a phase range of 0.1 of pulsar rotational period, centered on the pulsed emission. Panels (A), (B) and (C) present observations at 680 MHz, 1390 MHz and 3030 MHz respectively, showing the similarity of the intensity variation over the wide frequency range. The vertical line at longitude 270° represents the longitude of inferior conjunction of B (i.e. the orbital phase at which B is closest to the Earth).

inferior conjunction, when pulsar A is between B and the observer. Note that the 4-minute discovery observation of J0737−3039A has an orbital longitude of 146°, where B is faint: this explain why J0737−3039B wasn't detected in the survey data.

PSR J0737−3039B has a really unusual behavior not only as far as the emission strength, but also in pulse profile. In striking contrast with what observed in any other binary pulsar, the pulse profile varies along the orbit.

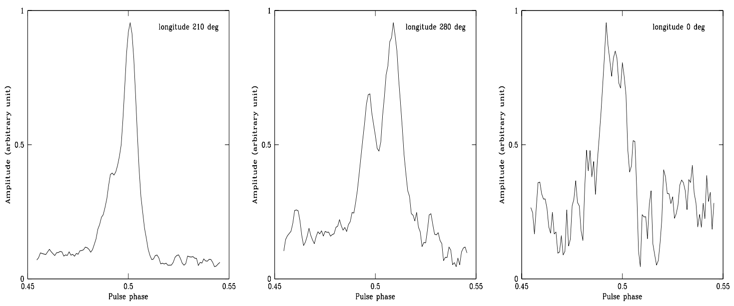

Figure 4.8: Pulse profiles for PSR J0737−3039B at different orbital phases.

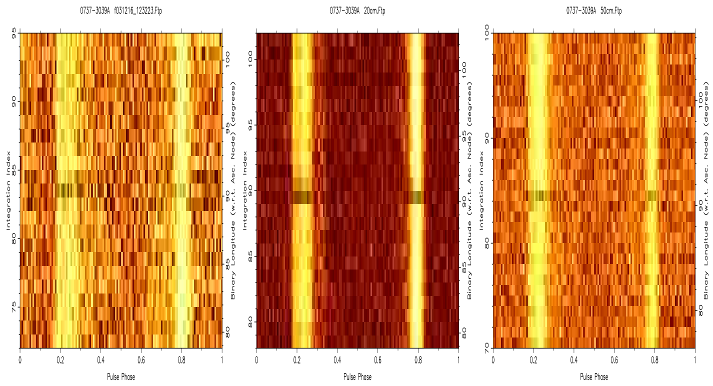

Figure 4.6: Pulse phase vs orbital longitude relative to the ascending node for a subsection of the orbit of PSR J0737−3039A. The eclipse is visible in all three panels, showing, from left to right, pulses at 10, 20 and 50 cm, around longitude 90°.

In pulsar A a $\sim$ 30 second eclipse is seen in the orbital longitude range $89° - 91°$, corresponding to the superior conjunction (i.e. when pulsar A is behind B). Figure 4.6 shows, for observations taken at 10 (left panel), 20 (central panel) and 50 cm (right panel), J0737−3039A pulses over roughly ten minutes, from orbital longitude $\sim 80°$ to $\sim 100°$. At all the three adopted wavelengths the short eclipse is seen: it's shape and duration seem to be frequency independent.

PSR J0737−3039B displays an even more puzzling behavior. Figure 4.7 shows the strength of the 2.8-s pulsed emission in the three frequency bands used for the observations (top is 10 cm, middle is 20 cm and bottom is 50 cm), as a function of orbital phase over the full orbit. The flux density received from B is dramatically changing along the orbit: the signal is clearly visible for two brief periods of about 10 minutes duration each centered on orbital longitudes 210° and 280°. Within these bursts the strength of the emission is such that most pulses are detected individually. In addition to orbital phases where the signal is strong, the pulsar often shows weaker emission elsewhere (in figure 4.7 a faint signal can be seen between orbital longitudes $\sim 0°$ and $\sim 20°$). Observations made with the Green Bank Telescope (GBT, Ransom private communication) showed that pulsar B's emission is present along almost all the orbit becoming apparently undetectable (eclipsed?) only at

2.2.1 Processing

The first stage of processing consists in the identification of spurious signals in the power spectrum of non de-dispersed (zero-DM) data set. Radio Frequency Interferences (RFIs), being produced mainly on Earth, are indeed often undispersed. Known signals as, for instance, the power line at 50 Hz and its harmonics, are firsts identified and their bandwidth determined. The remaining spectrum is searched for signals that appears many times in different positions in the sky: if a frequency is seen in more than four beams of a pointing or if it appears three times in the same beam of different pointings or if it appears more than seven times in the whole tape, it is flagged as an RFI. These signals and their harmonics are then deleted in the single pointing where they have been found or, for the last case, in the entire tape.

The subsequent step of the data analysis consists in the de-dispersion of the signal at different trial DMs. The 'Tree' algorithm (Taylor 1974) is used: the original time series, sampled every 125 μs is de-dispersed using DM values ranging from zero to the value corresponding to a broadening of the signal in a single frequency channel equal to the sampling time (i.e. from 0 to 17 pc cm^{-3}). Then the data samples are summed in pairs so that the new effective sampling time is double the original one. The rebinned time series is again de-dispersed as described above (hence with DMs ranging from 17 to 35) and the process is reiterated five more times. One then ends with seven `.dedisp` files containing time series de-dispersed with DM values from 0 to the minimum between 1088 (corresponding to a 4 ms smearing) and $42/\sin|b|$ pc cm^{-3} (the higher the galactic latitude b the smaller the amount of interstellar medium).

The de-dispersed time series are then Fourier transformed using a Fast Fourier Transform (FFT) routine. The resulting power spectra are harmonically summed in such a way that at each fundamental is added its first harmonic (fig 2.4). The harmonic summing process is particularly efficient for signals - as the radio pulsars ones - having narrow peaks: a pulse having width W will have approximately $P/2W$ harmonics with amplitude comparable to that of the fundamental, while a sinusoidal wave will have a large fundamental peak and small power in the harmonics.

The original power spectra and those obtained summing 2, 4, 8 and 16 harmonics are searched for significant peaks to give a set of 50 candidate periods (10 from the fundamental spectrum and 10 from each harmonic sum)

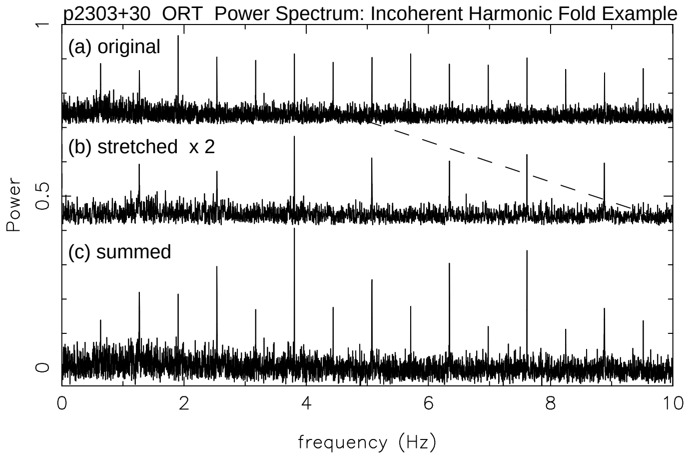

Figure 2.4: The first half of the power spectrum is stretched in such a way that at each fundamental is summed its first harmonic.

for each DM. For each candidate a pulse profile in the time domain is created by inverse transformation of the complex Fourier components for the fundamental and it's harmonics. For all the candidates having signal-to-noise ratios greater than four (to a maximum of 265 candidates per beam, sorted by S/N), the appropriate de-dispersed time series are summed in 4 sub-bands and folded in 32 to 64 sub-integrations (depending on the candidate period), each lasting ~ 8 to ~ 4 seconds, using the nominal period and dispersion measure. Sub-bands and sub-integrations are then summed with a range of delays in frequency and time, up to one sample per sub-band and per sub-integration, to search for the maximum S/N over a range of parameters around the nominal P and DM. The resulting profiles, the new maximised S/N ($P - DM$ signal-to-noise ratio) and related parameters are then stored for later inspection.

2.2.2 Results Inspection

In the last step of data reduction the candidates of an entire tape are compared and searched for common periods. If a signal appears more than six times in a tape, it is flagged as an interference. All the remaining candidates, having a $P - DM$ S/N greater than 8.0 (usually) are visually inspected using an

	PSR J0737−3039A		PSR J0737−3039B
B (G)	6.3×10^9		1.2×10^{12}
τ (Myr)	210		50
$\dot{E}$ (erg/s)	6000×10^{30}		2×10^{30}
d (kpc)		~ 0.6	
z (kpc)		~ -0.05	
M_f ($M_\odot$)	0.29097(1)		0.356(3)
$M_A + M_B$ ($M_\odot$)		2.588(3)	
M_A/M_B		1.069(6)	
M ($M_\odot$)	1.337(5)		1.250(5)
i (°, from s)		87(3)	
i (°, from R and $\dot{\omega}$)		87.7(-29, +17)	

Table 4.3: Derived parameters for PSR J0737−3039A and B. From top to bottom: surface magnetic field, characteristic age, spin-down energy, DM derived distance and height on the galactic plane, mass function, total system mass, mass ratio, stellar mass (from the measured mass ratio and $\dot{\omega}$ and using eq. 4.1), orbital inclination (derived from timing fit of the Shapiro delay s), orbital inclination (from the measured mass ratio and $\dot{\omega}$ and using eq. 4.1). The 2-σ errors on the last quoted digit(s) are given in parenthesis.

To be fully consisted with the model presented above both pulsars should have the same age: the (re-)birth of the millisecond pulsar should be roughly coincident with the end of the mass transfer phase and with the supernova explosion, hence with the birth of the second pulsar. The characteristic ages of PSR J0737−3039A and B, on the contrary, differs by a factor ~ 4. This discrepancy can be easily reconciled by questioning one or more of the assumptions inherent in the calculation of characteristic ages: a negligible birth spin period and a magnetic dipole braking torque (see eq. 1.5 and 1.6). At very least, the initial (post-accretion) spin period of PSR J0737−3039A cannot have been negligible with respect to the present value: at most, the accretion could have pushed it up to the spin-up line (as explained in §1.3). If we simply assume a constant magnetic field and a constant dipole spin-down after the end of the accretion, we can calculate that the initial rotational period value should have been in the range $10 - 18$ ms (Lyne et al. 2004), enough to explain the characteristic age discrepancy.

4.2.2 Eclipses and Intensity Variations

Another intriguing property of PSR J0737−3039A and B, whose implications are investigated in §4.3.3, is the fact that both show eclipses and/or variations in the emitted flux.

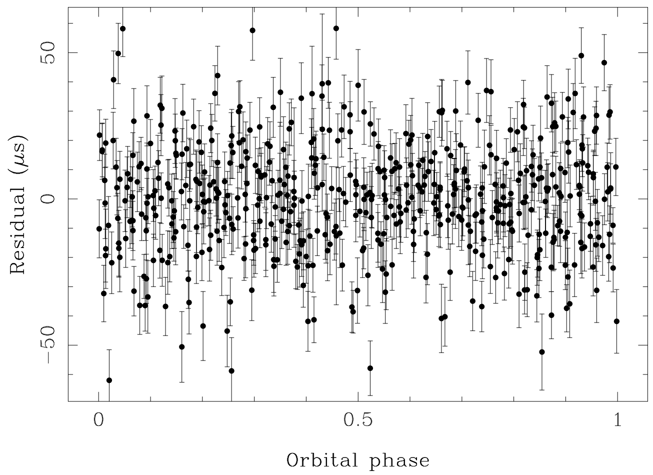

Figure 4.4: Timing residual plotted versus orbital phase for PSR J0737−3039A.

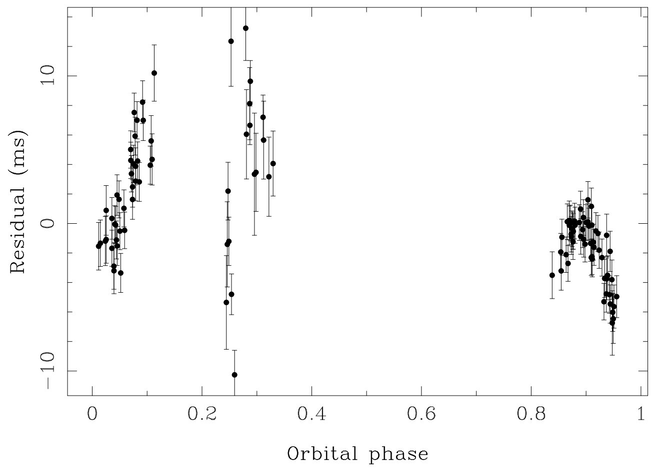

Figure 4.5: Timing residual plotted versus orbital phase for PSR J0737−3039B.

interactive display (`runview` fig. 2.5) and classified as Class 1 or Class 2 candidates or rejected as interferences (Class I).

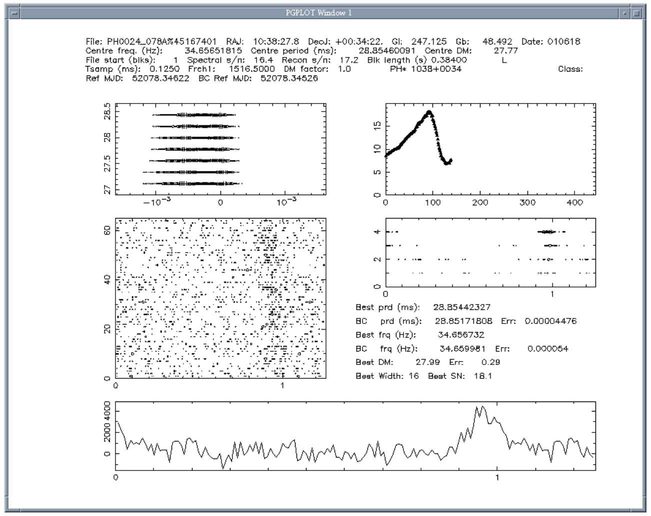

Figure 2.5: `Runview` output plot for a Class 1 candidate subsequently confirmed as the pulsar PSR J1038+0034. Clockwise from the top left the sub-plots show a gray-scale of the dependence of S/N on DM and offset (in ms) from the nominal period, the dependence of S/N on DM trial number, a grey-scale plot of S/N vs pulse phase in four sub-bands, the integrated pulse profile and a grey-scale plot of S/N vs pulse phase for 64 sub-integrations.

Although the classification of candidates is somehow subjective, there are several features characterizing a pulsar signal that one can search for in the `runview` plots: a high $P - DM$ signal-to-noise ratio, together with a well defined peak in the DM vs S/N plot and continuity of the pulse signal across sub-bands and sub-integrations are the most important criteria to discriminate between real pulsars and an RFIs. The signal should also be linear or parabolic (indicating a constant acceleration) in the phase-time plot and linear in the phase-frequency one (see fig. 2.5 caption).

2.2.3 Candidate Confirmation: gridding and `binary-confirm`

Once a Class 1 candidate is selected it is necessary to confirm it's pulsar nature. To do so the suspect is observed at 5 grid positions, one at the nominal

coordinates and four with an offset in latitude and longitude of 9 arcminutes, using the central beam of the multibeam receiver. These observations are searched in period and dispersion measure around the nominal values and, if two or three detections are obtained, an improved position is computed from the relative signal-to-noise ratios. This technique is known as “gridding” of a suspect.

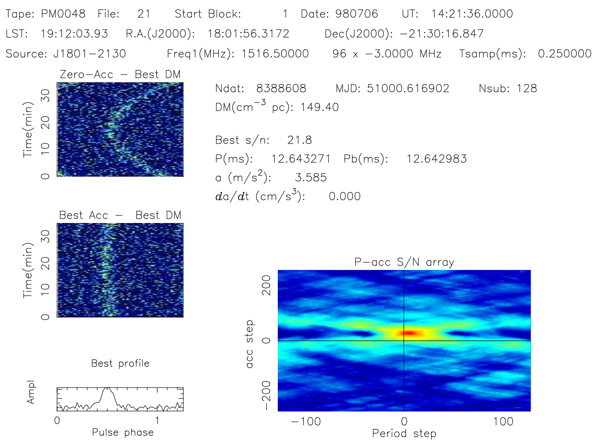

Figure 2.6: `Binary-confirm` output plot for the binary pulsar PSR J1801−2130. On the left: top panel shows the phase vs sub-integrations plot before the phase shift correction, below the same plot after the correction and at the bottom the pulse profile after correction. On the right: period step (centered on the input period in ms) vs acceleration step (centered on 0.0 m/s^2); the colourscale (from blue to red) indicates increasing S/N.

For millisecond candidates, if there is no detection, the central pointing is searched for parabolic shifts in phase. If the pulsar belongs to a tight binary system, indeed, the simple linear $P - DM$ search approach doesn't work because *(i)* the period can be significantly different from the nominal one (hence not searched) and *(ii)* the integrated pulse can be completely smeared out summing in phase sub-integrations where the phase of the signal is not constant (Doppler shifted). To perform such a search the programme `binary-confirm` is used. After the de-dispersion of the data `binary-confirm` launches, with different values of the input period, a programme that searches, over 128 sub-integrations, for the best linear or parabolic shift (i.e. the phase

PSR	J0737−3039B
RAJ	07:37:51.2472(13)
DECJ	−30:39:40.74(4)
PEPOCH (MJD)	52870.00000
P (ms)	2773.4607474(4)
$\dot{P}$	0.88(13) × 10^{-15}
DM (pc/cm^{-3}	48.7(2)
P_b (d)	0.1022515630(11)
$a \sin i$ (lt-s)	1.513(4)
e	0.087778(5)
$T0$ (MJD)	52870.0120588(6)
ω (°)	73.805+180.0
$\dot{\omega}$ (°/yr)	16.902(14)
γ (ms)	0.00038(6)
s	0.9995(-32, +4)
r (μs)	5.6(-12, +18)
NTOA	112
SPAN MJD	52760 – 53066
RMS (μs)	2660

Table 4.2: Measured parameters for PSR J0737−3039B over ∼ 10 months of timing. The 2-σ errors on the last quoted digit(s) are given in parenthesis.

Figures 4.4 and 4.5 show the timing residuals for PSR J0737−3039A and PSR J0737−3039B respectively plotted versus the orbital phase. As will be described in §4.2.2, pulsar B is clearly visible only for two (or three) brief period around phases 0.1, 0.9 and occasionally 0.3. Delays in the signal are also seen in the three different high visibility phases.

The importance and uniqueness of the timing measurements obtained for these two objects are presented in §4.3.1.

The derived parameters for both pulsars are given in table 4.3. It is important to point out that spin period and magnetic field of the two pulsars nicely agrees with what predicted by the standard evolutionary model for the formation of Double Neutron Stars (e.g. Bhattacharya & van den Heuvel 1991). According to this model, in fact, the first born neutron star (in this case pulsar A), having accreted matter from a massive companion, has been spun-up to millisecond periods and its magnetic field (according to the scenario presented in §1.3) has been somehow reduced by the accretion itself. When the companion star explodes in a supernova it becomes the second neutron star of the system (here B). Since this second-born neutron star is not subjected to any mass transfer on its surface, it is expected to be a 'normal' pulsar, with a long period and a high magnetic field. PSR J0737−3039B nicely fits this picture providing confirmation of the standard scenario.

PSR	J0737−3039A
RAJ	07:37:51.2472(13)
DECJ	−30:39:40.74(4)
PEPOCH (MJD)	52870.00000
P (ms)	22.69937855615(6)
$\dot{P}$	$1.74(5) \times 10^{-18}$
DM (pc/cm^{-3}	48.914(3)
P_b (d)	0.1022515630(11)
$a \sin i$ (lt-s)	1.415036(17)
e	0.087778(5)
$T0$ (MJD)	52870.0120588(6)
ω (°)	73.805(3)
$\dot{\omega}$ (°/yr)	16.902(14)
γ (ms)	0.00038(6)
s	0.9995(-32, +4)
r (μs)	5.6(-12, +18)
NTOA	538
SPAN MJD	52760 – 53066
RMS (μs)	27

Table 4.1: Measured parameters for PSR J0737−3039A over $\sim$ 10 months of timing. The 2-σ errors on the last quoted digit(s) are given in parenthesis.

Table 4.2 gives the list of parameters obtained from the timing of pulsar B over $\sim$ 10 months. Since the timing results for a millisecond pulsar are usually by far more precise than what we can obtain for long period objects, the parameters that the two pulsars have in common (position, orbital period, eccentricity, epoch of periastron, advance of periastron, rate and shape of Shapiro delay) are derived from the timing solution of pulsar A. The longitude of periastron for J0737−3039B is obtained simply adding 180° to the value measured for J0737−3039A.

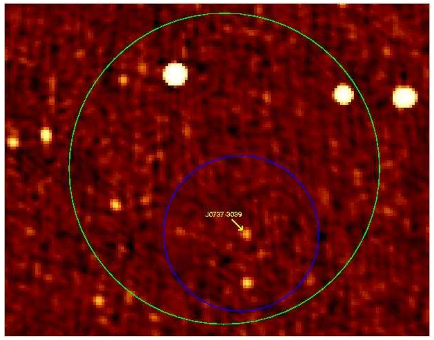

Figure 4.3: NVSS map @1.4 GHz. The green circle gives the original detection position, blue circle is the refined gridding position.

shift that gives the highest signal-to-noise ratio). The best period step ps and range pr for launching the search programme, given the input parameters (nominal period, sampling time and observation length), are calculated in such a way that the difference ps between an input period and the following one produces a maximum phase shift corresponding to a broadening of the pulse in one sub-integration of one phase bin (one sample, typically), i.e. to a total shift of 128 bins over the whole observation. The period range over which the search programme is launched (i.e. the maximum variation of the period from the nominal value that we consider) is chosen in such a way that $pr/P_i = 0.001$ (where P_i is the ith input period). An example of a `binary-confirm` output plot is shown in figure 2.6.

2.3 Timing

When a new pulsar is discovered and confirmed the only known parameters are its approximate position (within few arcminutes), rotational period P and dispersion measure DM, that gives a rough estimate of the pulsar's distance, once a model for the electrons' distribution in the Galaxy (e.g. Taylor & Cordes 1993) is assumed.

A follow-up observational campaign then starts in order to better assess new pulsars' positions and rotational parameters (P and $\dot{P}$). These quantities allow to estimate the pulsar age and magnetic field and to cross-correlate its position with that of possibly related sources, such as X-ray or γ-ray objects or supernova remnants. The regular monitoring ('timing') of new discoveries also allows to determine whether a pulsar is isolated or belongs to a binary system and, in the latter case, to derive its orbital parameters.

Timing a pulsar means measuring and phase connecting the pulses times of arrival (TOAs). To do so, a standard profile (obtained summing in phase an adequate number – $\gtrsim$1000 – of single pulses) is convolved with the integrated profiles of each observation: the topocentric TOA is then calculated adding at the starting time of the observation the fraction of period, τ, at which the χ^2 of the convolution is minimised.

The measured times are then compared with TOAs predicted by a given pulsar model. The best fit positional, rotational and orbital parameters are then obtained minimizing the differences between measured and predicted times of arrivals (the timing residuals) with a multiparametric fit.

The first step of a timing analysis is the transformation of the topocentric TOAs to the Solar System baricenter, in first approximation an inertial reference frame.

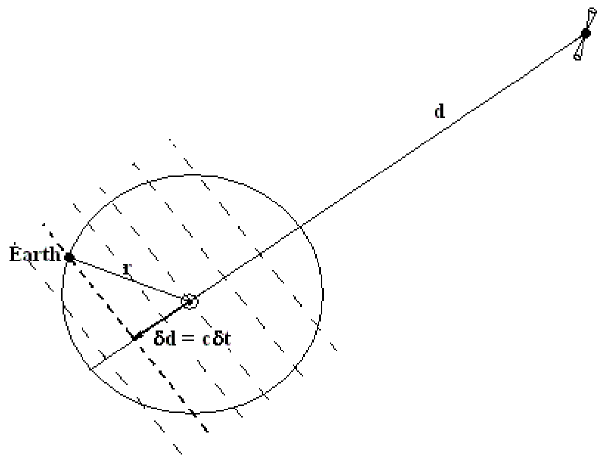

Figure 2.7: Correction from topocentric to baricentric coordinates: TOAs must be corrected for δt, the time necessary to the wavefront to cover the distance δd.

The time correction takes into account the Roemer delay $\Delta R_{\odot}$ (due to the motion of the Earth), the delays due to the dispersion in the ISM and the corrections due to the relativistic effects known as Einstein delay $\Delta E_{\odot}$ and Shapiro delay $\Delta S_{\odot}$). In summary the baricentrised TOA t_b is obtained applying the formula:

$$t_b = t + \Delta R_{\odot} - \frac{D}{\nu^2} + \Delta E_{\odot} - \Delta S_{\odot} \tag{2.3}$$

where t is the topocentric TOA. The Roemer delay can be written as

$$\Delta R_{\odot} = \frac{\mathbf{r}\cdot\mathbf{n}}{c} + \frac{\mathbf{r}\cdot\mathbf{n} - |r|}{2cd} \tag{2.4}$$

where $\mathbf{n}$ is the versor on the line going from the Sun to the pulsar and $\mathbf{r}$ is the vector connecting the Sun and the Earth. The second term in equation 2.3 takes into account the delay introduced by the dispersion (see §1.4.1). Here D

(or simply 'B'), had the same dispersion measure as PSR J0737−3039A (or 'A'), and showed orbital Doppler variations that identified it, without any doubt, as the companion to the millisecond pulsar. The first ever Double Pulsar system had been eventually discovered.

The timing parameters and the observational characteristic of the two pulsars are given in §4.2.1. As will be described in §4.2.2, pulsar B was not detected in the 4-minute survey integration because its signal is clearly visible for only $\sim$ 20% of the orbit. The discovery of such a unique system has important implications in many fields of astrophysics: in §4.3.1 the importance of the discovery of PSR J0737−3039A and B in testing relativistic gravity is shown, in §4.3.2 the repercussions on the possibility to detect gravitational waves are described and in §4.3.3 the unique possibilities given by the peculiar emission of the pulsars in this system (see §4.2.2) to investigate pulsars' magnetospheres and to test emission mechanisms are explained.

4.2 PSR J0737−3039A and B: Observational Characteristics

In this section the measured parameters and main characteristics of PSR J0737−3039A and B are summarised. The interpretation and implications of the properties of the pulsars are presented in §4.3.

4.2.1 Timing Results

Table 4.1 gives the best fit parameters obtained using the Damour & Deruelle model (1986) from the timing of pulsar A over $\sim$ 10 months.

In order to obtain a coherent timing solution over the few initial months of observation (from which deriving the spin period derivative of PSR J0737−3039A), it has been necessary to perform an independent measurement of the pulsar's position. Inspecting NVSS catalogue and maps, a point-like source with $\sim$ 20% of linearly polarised flux density was found in the $7'$ gridding error circle (see fig. 4.3). To confirm this likely identification and improve the positional accuracy, in June 2003 a $\sim$ 5 hours observation was performed at the Australian Telescope Compact Array (ATCA) in Narrabri (NSW, Australia) yielding the pulsar's position with arcsecond precision. After collection of data spanning $\sim$ 10 months, also a positional term was fitted to the times of arrival, allowing to further improve the accuracy of the pulsar location in the sky.

where m_1 and m_2 are the two star masses (in our case they correspond to M_{NS} and M_c), $M = m_1 + m_2$, $x = a \sin i$ and $T_\odot \equiv GM_\odot/c^3 = 4.925490947\,\mu$s. The parameter $\dot{\omega}$, as just mentioned, measures the advance of the periastron, γ is a term taking into account gravitational redshift and time dilatation, $\dot{P}_b$ is the so-called orbital decay and measures the rate at which the orbital period decreases due to losses of binding energy via gravitational radiation. Finally, r and $s \equiv \sin i$ are respectively the rate and the shape of the Shapiro delay, a parameter measuring the time delays of the signal caused by the space-time deformations around the companion star.

The measured value of $\dot{\omega}$ implied a total mass for the system containing PSR J0737$-$3039A of about 2.58 M$_\odot$ giving a maximum mass for the pulsar of about 1.34 M$_\odot$ and a minimum mass for the companion $\sim$ 1.24 M$_\odot$. While the maximum mass for the pulsar perfectly agrees with the other measurements of neutron star masses (Thorsett & Chakrabarty 1999), the mass of the companion is a little lower than average. In absence of additional information the white dwarf hypothesis could not be completely rejected. It is important to point out, anyway, that the $\dot{\omega}$ value that one measures, in general, is given by the term of equation 4.1 plus two classical extra terms, arising *(i)* from tidal deformations of the companion star (relevant only if the companion is non degenerate) and *(ii)* from rotationally induced quadrupole moment of the companion star, applicable to the case of a fast rotating white dwarf. For a neutron star both the additional contributions are negligible. If the companion to J0737$-$3039A was a white dwarf the relativistic $\dot{\omega}$, and by consequence the total system mass, would be smaller than the measured one (since $\dot{\omega}_{GR} = \dot{\omega}_{obs} - \dot{\omega}_{classical}$) implying an implausibly small ($\lesssim$1 M$_\odot$) maximum allowed mass for J0737$-$3039A (that, being a pulsar, is certainly a neutron star).

All these pieces of evidence strongly suggested that the discovered binary was the sixth, and by far the most relativistic, Double Neutron Star system known (see §4.3.1 for the implications of its discovery for testing relativistic gravity).

The ultimate confirmation of the above picture came few months later when, analysing the follow-up observations of PSR J0737$-$3039A, a strong signal with a repetition period of $\sim$ 2.8 seconds occasionally appeared (Lyne at al. 2004). The newly discovered pulsar, henceforth called PSR J0737$-$3039B

is the so-called dispersion constant defined as:

$$D = \frac{t_2 - t_1}{\nu_2^{-2} - \nu_1^{-2}} = \frac{e^2}{2\pi m_e c}\int_0^d n_e dl \qquad (2.5)$$

Einstein's delay is a combination of gravitational redshift and relativistic time delay due to the motion of the Earth and the other solar system's planets. It's derivative is given by:

$$\frac{d\Delta E_\odot}{dt} = \sum_i \frac{Gm_i}{c^2 r_i} + \frac{v_\oplus^2}{2c^2} \qquad (2.6)$$

where G is the gravitational constant, m_i are the masses of the planets, r_i their distances to the Sun and $v_\oplus$ the velocity of the Earth with respect to the baricenter of the solar system. The Shapiro delay (Shapiro 1964) measures the propagation time of an electromagnetic wave in the gravitational field of the Sun. This quantity is a function of the angle θ from the pulsar to the Earth and the Sun:

$$\Delta S_\odot = -\frac{2GM_\odot}{c^3}\log\left(1 + \cos\theta\right) \qquad (2.7)$$

If the pulsar is orbiting a companion star, the TOAs vary along the orbit anticipating when the pulsar is in front of the companion and delaying when it's behind it (orbital Doppler variations). Fitting for the orbital modulations one can hence derive five keplerian parameters describing the binary system: the orbital period P_b, the eccentricity e, the projection of the semi-major axis $x = a \sin i$, the periastron longitude ω and the epoch of periastron T_0. Combining these quantities one can derive the *mass function*:

$$f(M) = \frac{(M_c \sin i)^3}{(M_{NS} + M_c)^2} = \frac{4\pi^2 (a \sin i)^3}{GP_b^2} \qquad (2.8)$$

where M_c is the companion mass. Assuming a typical value for $M_{NS} = 1.4$ M$_\odot$ and an edge on orbit ($i = 90°$) we can obtain a lower limit for the companion mass.

When a pulsar is in an eccentric orbit along a compact massive companion (producing a strong near gravitational field), up to five further parameters – the so-called post-keplerian parameters – can be measured (see §4).

From the practical point of view timing a pulsar means comparing the baricentrised TOAs with the ones predicted by a model describing rotational, positional and orbital parameters of the given pulsar and searching for systematic trends in the time residuals.

A bad estimate of the spin period, for instance, will give a linear trend in the timing residuals (fig. 2.8) and an error in the period derivative will give a parabolic trend (fig. 2.9).

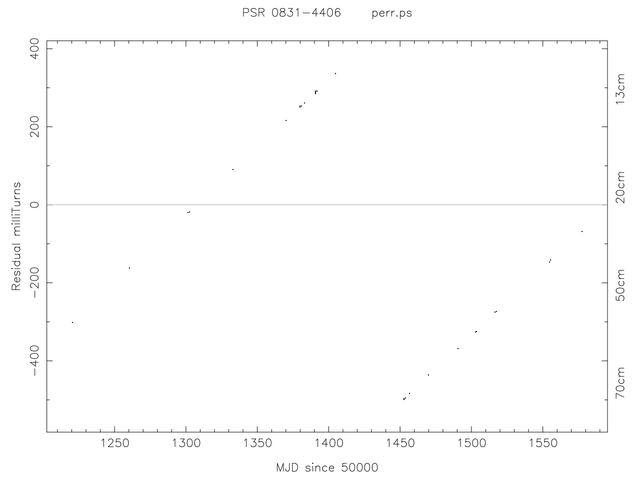

Figure 2.8: Timing residuals with an error in the estimate of the spin period.

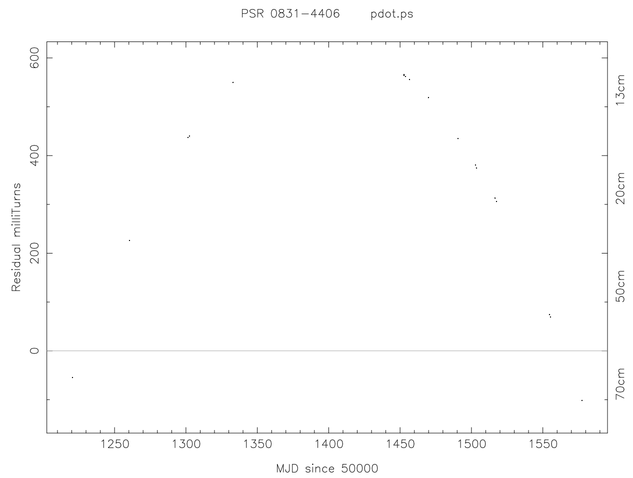

Figure 2.9: Timing residuals with an error in the estimate of the period derivative.

a second neutron star. The first hypothesis could be immediately ruled out since the radius of a non degenerate object of the required mass would almost completely fill the orbit of the system, probably producing deep and extended eclipses or, at least, strongly affecting the radio emission, which is not seen in the signal of PSR J0737−3039A. On the other hand, also the CO-WD scenario appeared unlikely considering the eccentricity of the orbit: a system containing a recycled neutron star and a white dwarf is indeed expected to be highly circular since it had the time to reach the minimum energy configuration (i.e. to circularise). If a second, recent supernova explosion has occurred forming another neutron star, the energy and momentum released would have distorted the system and this would explain the observed eccentricity.

A further strong constraint on the mass of PSR J0737−3039A companion came few days later from the first fit of a binary model to the times of arrival of the pulsations. By using a data span of only 6 days, a 10-σ determination of the advance of the periastron, $\dot{\omega}$, was possible. This parameter resulted to have an extraordinarily high value: $\dot{\omega} \sim 17$ °/yr (note that the the previously highest observed value for this parameter was 5.33 °/yr, measured for PSR J1141−6545, Kaspi et al. 2000).

The periastron advance is one of the five post-keplerian parameters (see §2.3) that can be used to describe the corrections to the classical laws of orbital motion and signal propagation when the emitting source travels in a strong gravitational field.

In any given theory of relativistic gravity, the post-keplerian (PK) parameters can be written as function of the pulsar and companion masses and of the keplerian parameters. In the case of General Relativity, the equations describing the PK parameters assume the form (Damour & Deruelle 1986, Taylor & Weisberg 1989, Damour & Taylor 1992):

$$\dot{\omega} = 3\left(\frac{P_b}{2\pi}\right)^{-5/3} (T_\odot M)^{2/3}\,(1-e^2)^{-1} \tag{4.1}$$

$$\gamma = e\left(\frac{P_b}{2\pi}\right)^{1/3} T_\odot^{2/3}\,M^{-4/3}\,m_2\,(m_1+2m_2) \tag{4.2}$$

$$\dot{P}_b = -\frac{192\pi}{5}\left(\frac{P_b}{2\pi T_\odot}\right)^{-5/3}\left(1+\frac{73}{24}e^2+\frac{37}{96}e^4\right)(1-e^2)^{-7/2}\,\frac{m_1\,m_2}{M^{1/3}} \tag{4.3}$$

$$r = T_\odot\,m_2 \tag{4.4}$$

$$s = x\left(\frac{P_b}{2\pi}\right)^{-2/3} T_\odot^{-1/3}\,M^{2/3}\,m_2^{-1} \tag{4.5}$$

massive companion. Right panel of figure 4.1 shows the result of the analysis of the same 4-minutes data processed with the `binary-confirm` code (§2.2.3). This programme found the best correction to the Doppler phase shift for an acceleration of 99 m/s^2 suggesting a binary period of just few hours for a companion of $\sim$ 1 M$_\odot$ (as a comparison, the typical observed binary pulsars having a $0.2 - 0.3$ M$_\odot$ white dwarf companion display acceleration $\lesssim$50 m/s^2). After correction, the signal-to-noise ratio increases by $\sim$ 30% with respect to the detection value.

Follow-up observations performed in May 2004, consisting in three $\sim$ 5-hours integrations, confirmed that the orbit is indeed very tight and far from being circular: the binary period P_b is only 2.4 hr and the eccentricity $e \sim 0.09$. That makes J0737−3039A's orbit the tightest among those of all known binary pulsars in eccentric systems. Figure 4.2 shows the radial velocity curve obtained plotting the (barycentric) spin period of the pulsar, measured at different times, versus the binary phase: the fact that the orbit is eccentric can be easily argued from the asymmetric shape of that curve.

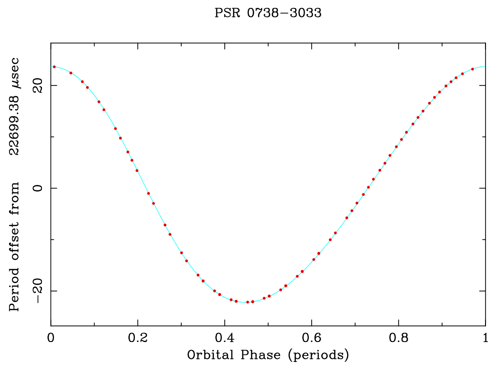

Figure 4.2: Radial velocity curve for PSR J0737−3039A.

From the orbital parameters available at that time ($P_b \sim 2.4$ hr, $a \sin i \sim$ 1.4 lt-s; for the current best estimates of these parameters see table 4.1), the pulsar mass function was calculated and resulted $M_f = 0.29$ M$_\odot$, implying a minimum companion mass of about 1.24 M$_\odot$, assuming $M_{NS} = 1.35$ M$_\odot$. Given such a high value for the minimum mass one could examine three possible hypotheses for the nature of the companion star: it could be a non degenerate object, a massive Carbon-Oxigen white dwarf (CO-WD) or

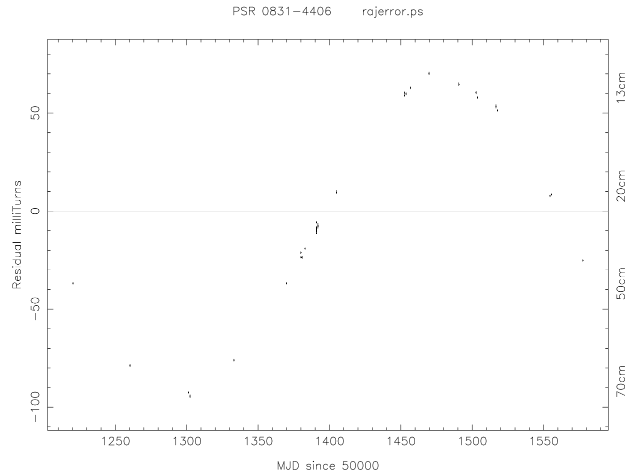

Figure 2.10: Timing residuals with an error in the estimate of the position.

Collecting TOAs for roughly a year allows to determine accurately the pulsar position. An error in the position, in fact, corresponds to an error in the baricentric TOAs correction and gives rise to a sinusoidal trend with a

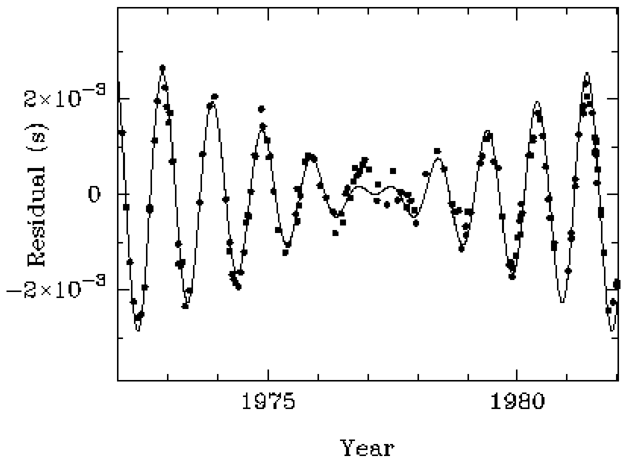

Figure 2.11: Timing residuals with proper motion set to zero.

period of one year in the residuals (fig. 2.10).

Continuing the timing observations over a period of several years also allows to measure the pulsar proper motion. In fact the changing position of the pulsar produces a sinusoidal modulation of the residuals with a period of a year and with increasing amplitude (fig. 2.11).

2.3.1 Timing Instabilities

After applying a correct timing model, one would expect a set of uncorrelated timing residuals randomly scattered about a zero mean value. This is not always the case: the residuals of many pulsars, mostly the youngest ones (Manchester & Taylor 1974, Cordes & Helfand 1980), exhibit quasi-periodic variations with time (fig. 2.12) known as "timing noise".

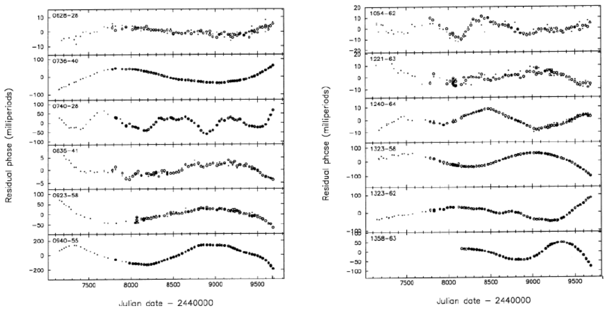

Figure 2.12: Examples of noisy timing residuals (D'Alessandro et al. 1995).

Millisecond pulsars, on the contrary, are very stable clocks and are virtually not affected by timing instabilities.

While the physical processes of this phenomenon are not well understood, it seems likely that it may be connected to superfluid processes and temperature changes in the interior of the neutron star (Alpar, Nandkumar & Pines 1986), or processes in the magnetosphere (Cheng 1987a, Cheng 1987b).

Chapter 4

The Double Pulsar J0737−3039

4.1 The Discovery

PSR J0737−3039A, a millisecond pulsar with a spin period of 22.7 ms, was discovered in April 2003 (Burgay et al. 2003). The original detection plot is shown in the left panel of figure 4.1. From the very pronounced curvature in the phase vs sub-integrations box (see §2.2.2 for a full description of output plots), denoting a time depending change in the phase of arrival of the pulses, it was immediately clear that the pulsar signal was affected by a significant Doppler effect in only 4 minutes of integration. That in turn suggested that the pulsar was experiencing the gravitational pull of a nearby and relatively

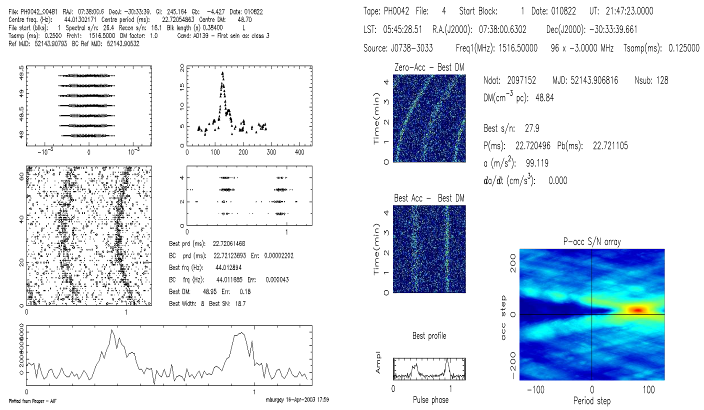

Figure 4.1: Left panel shows the original detection plot for PSR J0737−3039A. Right panel shows the same 4-minutes data analysed with `binary-confirm`.

of the two other DRPs and lower than that of the five pulsars belonging to a Double Neutron Star (DNS) system that were known at the time of J1038+0034 discovery, recently two other pulsars orbiting another neutron star have been found to have a period similar to that of J1038+0034 (Burgay et al. 2003, Faulkner et al. in preparation) making it very likely to be an 'aborted' DNS.

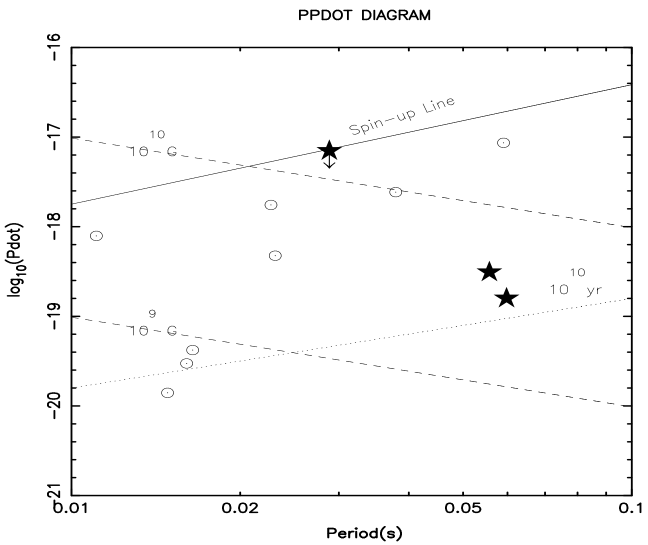

Figure 3.22: Zoom on the $P - \dot{P}$ diagram. Dots surrounded by a circle are binary pulsars. The three DRPs, the only isolated objects in this section of the diagram, are represented as filled stars. For PSR J1038+0034, whose period derivative is still unknown, we used the theoretical $\dot{P}$ upper limit in the likely hypothesis that this pulsar has been recycled, placing it on the spin-up line.

Chapter 3

Results

The analysis of the data of the Parkes High-Latitude Pulsar Survey (PH survey), collected in three years of observations starting from November 2000, resulted in the discovery of 17 new pulsars, four of which belonging to the class of millisecond, or recycled, pulsars. Of these, three are in a binary system, whose characteristics are described in detail in §3.2 and §4, and one is an isolated mildly recycled object (§3.3). Timing results for all the other pulsars are reported in §3.1.

PSR J	P (ms)	Date (MJD)	RAJ (h, m, s)	DECJ (°, ′, ″)	Beam	DM (pc cm^{-3})	S/N
0343−3000	2597.090	51950	03:43:48	−29:58:20	6	19.7	42.7
0610−2100	3.861	52146	06:10:24	−21:01:51	5	60.8	10.1
0636−4549	1984.491	52202	06:36:04	−45:48:31	1	30.9	11.2
0656−2228	1224.755	51984	06:56:59	−22:28:06	7	41.8	21.0
0719−2544	974.711	51985	07:18:41	−25:38:35	4	248.4	20.7
0726−2619	3442.632	52144	07:26:22	−26:19:14	7	109.5	15.1
0737−3033A	22.721	52143	07:38:00	−30:33:39	11	48.6	25.5
0737−3039B	–	–	–	–	–	–	–
0746−4529	2791.022	52357	07:46:59	−45:32:33	2	169.2	10.3
0818−3232	2161.176	51866	08:18:19	−32:34:38	2	144.7	54.4
0820−3921	1073.659	52080	08:20:56	−39:27:31	6	206.7	13.4
0821−4221	397.717	51943	08:21:01	−42:17:49	10	270.3	10.8
0838−2623	308.571	52854	08:38:58	−26:23:08	3	116.3	9.6
0843+0719	1365.859	52892	08:43:34	+07:19:02	11	36.6	15.9
0900−3144	11.109	52484	09:01:09	−31:45:38	10	76.1	20.8
1038+0034	28.582	52078	10:38:27	+00:34:22	10	28.0	18.1
1046+0301	326.266	52493	10:46:52	+03:01:34	10	46.2	25.5

Table 3.1: Original detection parameters for the 17 new pulsars discovered in the Parkes High-Latitude survey. Columns 1 to 7 gives the pulsar name, the discovery position (in equatorial coordinates J2000), the beam in which the pulsar has been found, the original dispersion measure value and signal-to-noise ratio. PSR J0737-3039B has been discovered using a different search code. Hence its discovery parameters cannot be compared with those of pulsars listed here (see §4.1).

The discovery parameters are given in table 3.1: in column 1 the name of each pulsar is listed, in columns 2 to 5 the date of the observation in Modified Julian Day (MJD), the nominal pointing position (J2000) of the discovery and the beam in which the pulsar has been discovered are given, whereas columns 6 and 7 report the original discovery dispersion measure DM and signal-to-noise ratio S/N. The full visual inspection of the results, as explained in §2.2.2 has been normally done for pulsar candidates having S/N greater than 8. All the discovery values of the signal-to-noise ratios listed in the above table are greater than 9.5, indicating that the adopted threshold is a reasonable choice. PSR J0737−3039B, as will be described in 4.1, has been discovered with a slightly different observing system and a different data reduction approach. It's discovery parameters aren't comparable with those of the other objects, hence are not listed here.

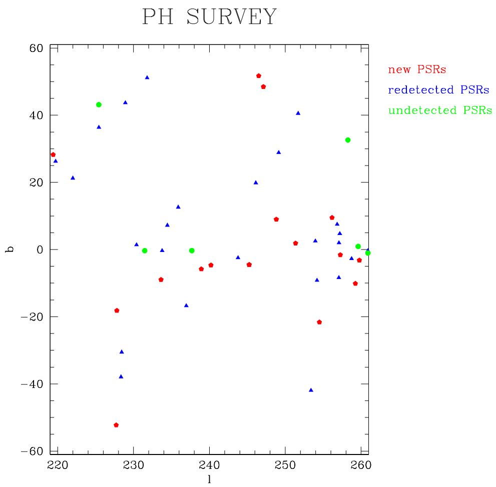

Figure 3.1: Survey area in galactic coordinates. Red points are the new discovered pulsars, blue triangles are the previously known objects re-detected by the present survey and green dots are the undetected ones.

All the previously known pulsars in the survey area, having a flux density above our sensitivity limit have been re-detected. Three of these are

In this case optical follow-up observations would be of great utility in order to assess the nature of the companion and also to compare the spin-down age of the pulsar with the cooling age of the white dwarf, (e.g. Serenelli et al. 2001) in order to better understand the evolution of this system. Helium white dwarfs are faint objects ($m_v \sim 25$) making desirable (compulsory) to employ optical telescopes of the class of 8 meters or the Hubble Space Telescope.

3.3 The New Isolated MSP J1038+0034

PSR J1038+0034 is a 28.8 millisecond pulsar. Unfortunately timing observations of this object are quite hard since its signal is heavily affected by interstellar scintillation. Although in the survey 4-minutes integration, dated June 2001, J1038+0034 appeared strong, with a signal-to-noise ratio of 18.1, since then only few and very spread good timing points have been collected. Flux is hugely varying in time making the pulsar undetectable even in integrations one hour long. Moreover between MJD 52490 and 52997 the pulsar has never been detected making even harder to obtain a coherent timing solution.

Before this gap in the data the timing residuals didn't show any evidence of a significantly high period derivative, which would have been seen if the pulsar was young, nor of any orbital modulation, suggesting that PSR J1038+0034 is a recycled and isolated pulsar. The relatively high value, in the context of millisecond pulsars, of the spin period suggests that the neutron star accreted only a small amount of mass from the former companion that then should have been a massive or an intermediate mass star.

All the other recycled pulsars having similar spin periods but two (PSR J2235+1506, Camilo, Nice & Taylor 1993, 1996 and PSR J0609+2130, Lorimer et al. 2004) belong to a binary system (see figure 3.22). The likely evolutionary scenario for these isolated pulsars is the so-called Disrupted Recycled Pulsar (DRP) scenario (Lorimer et al. 2004) according to which these objects are the first born neutron stars, spun-up during the short Roche Lobe overflow phase of their companions, of high mass binary systems that do not remain bound after the second supernova explosion.

This model seems to apply nicely to PSR J1038+0034 (if timing measurements will confirm its spin properties) making it the third object of the new class of DRPs. Although its spin period is roughly a half of that

(IMBPs, Camilo et al. 1996, 2001). The relatively longer-than-average spin period of MSP J0900−3144 is compatible with this hypothesis since the shorter evolutionary time scale of a massive star results in a lower amount of mass and angular momentum transfer on the neutron star surface, hence in a lesser spin-up. On the other hand the nature of the companion of J0900−3144 can be investigated by checking wether the binary system at which it belongs follows the relationship between eccentricity and orbital period found by Phinney et al. (1992) for Low Mass Binary Pulsars (LMBPs), systems in which the companion of the neutron star is a light Helium White Dwarf (He-WD), with orbital periods $\gtrsim$2 d. Plotting LMBPs and IMBPs on this diagram (figure 3.21, Camilo et al. 2001) we can clearly see that the latter class of objects, does not follow the predicted relationship. PSR J0900−3144, on the contrary, falls at the borders with the region containing 95% of LMBPs suggesting that its companion could be a somehow more massive than average He-WD.

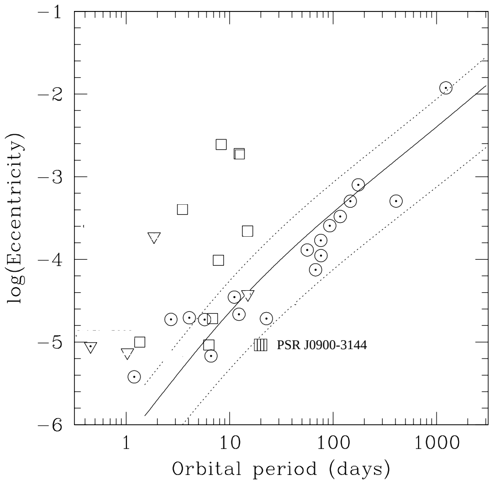

Figure 3.21: Orbital eccentricity vs orbital period of binary pulsars in the disk of the Galaxy with measured eccentricities $e < 0.1$. Empty squares are IMBPs and circles are LMBPs, triangles denotes upper limits on e. The dotted lines should contain 95% of the eccentricities of LMBPs according to the model of Phinney & Kulkarni (1994). PSR J0900−3144 is the filled square.

millisecond pulsars; the PH survey more than doubled the number of such sources in the selected region, fulfilling one of the main aim of this project, that is increasing the statistics on these objects. Figure 3.1 shows the region of the sky covered by the PH survey: the red points are the pulsars discovered during this work, the blue ones are the previously known re-detected pulsars and the green ones are the undetected ones, below our flux limits. The spatial distribution of millisecond pulsars, in previous large area surveys, appeared isotropic; in the present work, as well as in the intermediate and high latitude Swinburne surveys (Edwards et al. 2001, Jacoby et al. 2003), which have the same observational parameters as the PH survey, the millisecond pulsar population seems to be more concentrated in a latitude range $|b|\lesssim 20°$. This suggests that the flux limit for these surveys is low enough to sample the real spatial distribution of these sources and that the previously observed isotropy was essentially due to selection effects.

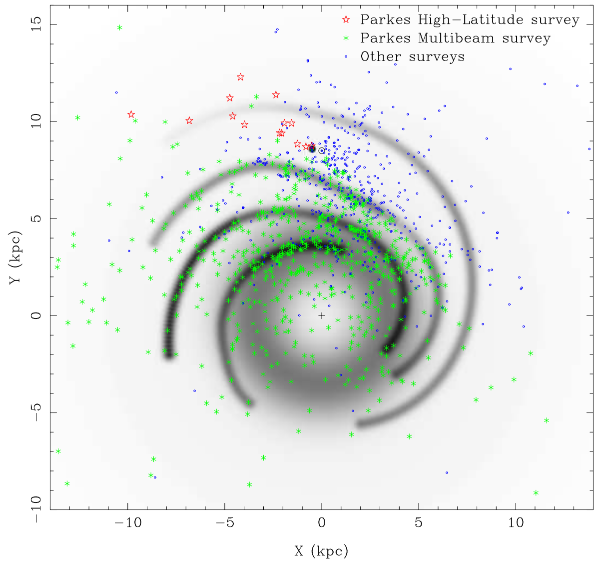

Figure 3.2: A cartoon of the Galaxy viewed from above. Red stars are the new discovered pulsars, green asterisks are the Parkes Multibeam survey pulsars (Manchester et al 2001, Morris et al. 2002, Kramer et al. 2003, Hobbs et al. 2004), blue dots are from other surveys.

Figure 3.2 shows the distribution in the Galaxy (seen from above the galactic plane) of new discovered and previously known pulsars. The new pulsars from the Parkes High-Latitude survey are plotted as red stars; green asterisks are the pulsars discovered in the Parkes Multibeam survey (Manchester et al 2001, Morris et al. 2002, Kramer et al. 2003, Hobbs et al 2004) and the blue dots are all the other known pulsars. The distance from the Sun has been derived using the dispersion measure and applying the electron density distribution model by Taylor & Cordes (1993).

It is worth noting that the new Parkes High-Latitude pulsars (PH pulsars) fill a previously poorly populated (and poorly searched) region of the Galaxy and, as pointed out by Kramer et al. (2003) for the Parkes Multibeam survey pulsars, they tend to follow the spiral arm structure. In this particular case the discovered pulsars trace the outer section of the Perseus spiral arm.

3.1 New Pulsars: Overall Characteristics

Table 3.2 shows the principal parameters obtained from the best fit of the timing data for the new discovered pulsars. All the timing analysis has been performed using the programme `TEMPO`[1]. First and second columns report the pulsar name and spin period for every object. When timing observations over more than one year were available, the period derivatives (column 3) and accurate positions (column 5 and 6 in equatorial coordinates) have been obtained. The reference epoch (in Modified Julian Day, MJD) for the reported period is listed in column 4. Column 7 gives the dispersion measure. For every tabled parameter, the numbers in parentheses are the 2–σ errors on the last quoted digit(s). For PSR J0719−2538 the reported values of position and period derivative is given with a 5-σ error since these two quantities are still covariant over the present data span.

Comparing tables 3.1 and 3.2, one can note that the original detection position has often a significant offset with respect to the real (or best fit) one resulting in a loss of signal in the original detection. It is worth noting, anyway, that the gridding procedure described in §2.2.3 gives a reliable estimate of the right position of the pulsar. Figure 3.3 shows, for a sample of the new pulsars, the discovery position (in green with an error circle of 1 beamwidth calculated at half power, i.e. $14'$), the gridding position (in blue with an error of half a

[1](http://www.atnf.csiro.au/research/pulsar/timing/tempo)

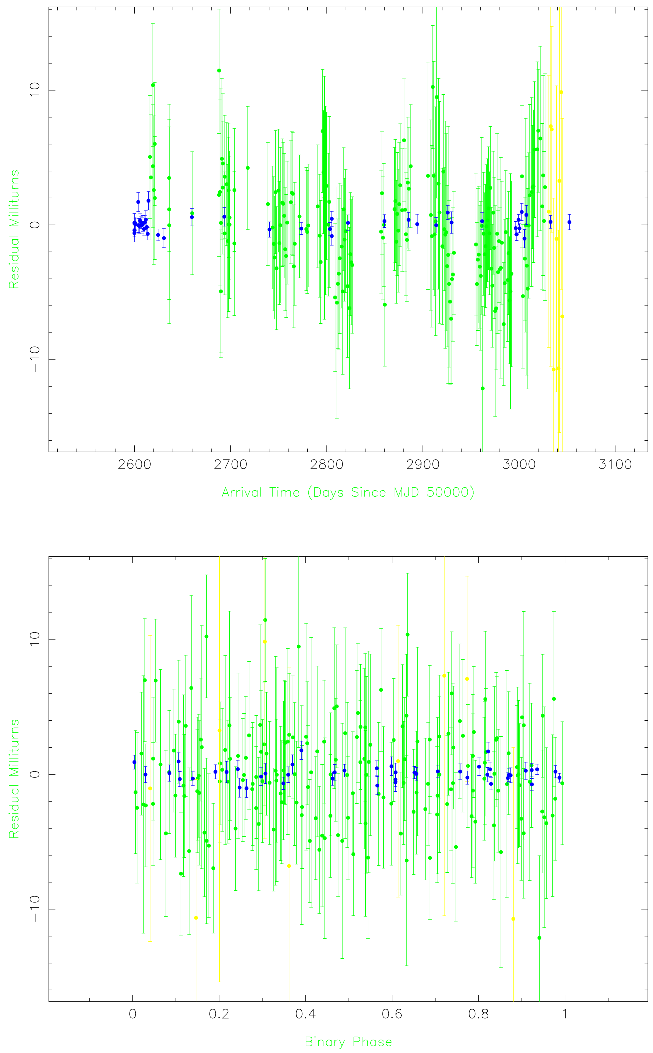

Figure 3.20: Timing residuals. Top panel shows residuals versus time (in MJD) and bottom panel, versus orbital phase. Blue points are the Parkes 20 cm data, green and yellow are Jodrell Bank data obtained respectively at 20 and 50 cm.

DECJ −31 44 26.4(88), totally consistent with our timing solution. The flux density reported for this source in the NVSS catalogue is 3.8(6) mJy with an integrated linearly polarised flux density of 1.77(84) mJy, again compatible with the point source to be a pulsar, whose typical values of the linearly polarised flux is $\sim$ 30% of the total flux density.

The mass function derived for the binary system containing PSR J0900−3144 is $M_f = 0.015693895(3)$ giving a minimum companion mass (adopting $M_{NS} = 1.35$ M$_\odot$) $M_c \geq 0.3577$ M$_\odot$. Assuming an inclination of the orbital plane $i = 60°$ and allowing the pulsar mass to be in the range 1.25 – 1.45 M$_\odot$ we obtain companion masses ranging from 0.4044 to 0.4423 M$_\odot$. As done for PSR J0610−2100, to give a more general view of what the mass function tells about the masses of the stars in the system, we plot in figure 3.19 the mass-mass diagram for J0900−3144.

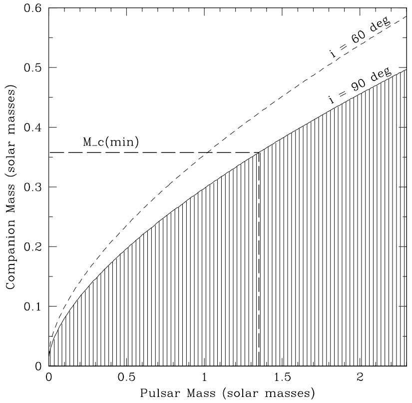

Figure 3.19: Mass-mass diagram for PSR J0900−3144. The shaded region is ruled out by the mass function, the dashed curve gives the masses of the two stars for an orbital inclination of 60°. Long-dashed lines indicate the minimum mass companion for a 1.35 M$_\odot$ neutron star.

The above calculations suggest that the companion of PSR J0900−3144 could be a Carbon Oxigen White Dwarf (CO-WD), whose typical mass is $\gtrsim$0.4 M$_\odot$, the minimum core mass for Helium flash. If this is the case we can argue that the progenitor of J0900−3144 companion was an intermediate mass star ($M_c \gtrsim 2$ M$_\odot$) and that J0900−3144 binary system is one of the few objects belonging to the relatively new class of Intermediate Mass Binary Pulsars

PSR J	P (s)	$\dot{P}$ (10^{-15})	PEpoch (MJD)	RA (J2000) (h, m, s)	DEC (J2000) (°, ′, ″)	DM (pc cm^{-3})
0343−3000	2.5970271565(3)	0.006(60)	52750.00	03:43:27.96(5)	−30:00:28.3(9)	19.7(1)
0610−2100	0.003861324704095(7)	1.6(6)e-05	52920.00	06:10:13.592(2)	−21:00:28.04(1)	60.67(2)
0636−4549	1.98459736721(15)	3.19(2)	52700.00	06:36:33.77(8)	−45:49:32.7(8)	30.9(1)
0656−2228	1.22475441479(7)	0.02(3)	52850.00	06:56:30.17(5)	−22:28:25.9(9)	41.8(1)
0719−2544	0.97472460475(12)	7.284(6)	52800.00	07:19:07.39(3)	−25:44:59.5(5)	248.4(1)
0726−2619	3.4426(4)	–	52144.00	07:26:22(1)	−26:19:14(1)	109.5(1)
0737−3039A	0.02269937855615(25)	0.0017(1)	52870.00	07:37:51.247(2)	−30:39:40.74(8)	48.914(3)
0737−3039B	2.7734607474(4)	0.88(13)	52870.00	07:37:51.247(2)	−30:39:40.74(8)	48.7(2)
0746−4529	2.7910248908(4)	16.74(7)	52750.00	07:46:59.42(7)	−45:29:27(1)	169.2(1)
0818−3232	2.16125892696(2)	0.75(1)	52500.00	08:18:25.93(1)	−32:32:30.8(2)	138.2(1)
0820−3921	1.07356658417(7)	12.175(9)	52700.00	08:20:49.07(8)	−39:21:55(1)	196.5(1)
0821−4221	0.396728145255(2)	3.4757(3)	52650.00	08:21:44.629(7)	−42:21:25.45(8)	266.5(1)
0838−2623	0.308571(4)	–	52854.00	08:38:19.72(1)	−26:22:14.5(1)	120.1(3)
0843+0719	1.36586(5)	–	52892.00	08:43:33.82(1)	+07:18:47.8(1)	36.6(3)
0900−3144	0.011109649156558(2)	4.83(7)e-05	52800.00	09:00:43.9525(2)	−31:44:30.913(4)	75.694(4)
1038+0034	0.02885155827(2)	–	52484.21	10:38:27(1)	+00:34:22(1)	26.4(1)
1046+0301	0.326266(4)	–	52493.00	10:46:52(1)	+03:01:34(1)	46.2(1)

Table 3.2: Measured parameters for 17 new pulsars discovered in the Parkes High-Latitude Pulsar Survey. Columns 1 to 7 report pulsar name, period, period derivative, epoch of the period measurement, right ascension and declination (J2000), dispersion measure. The values in parentheses give the 2-σ error on the last quoted digit(s) of the measured parameters. For PSR J0719−2538 the errors on the position and on $\dot{P}$ are given at 5-σ. Note that for J0343−3000 and J0656−2228 the period derivative is not yet constrained since the error is bigger than the value itself.

beamwidth) and the timing position (in cyan, with an error of 1′ for graphical purposes) overlayed on the NRAO VLA Sky Survey (Condon et al. 1998) maps at 1.4 GHz: gridding positions greatly agrees with the best fit ones.

Left and right panels of figure 3.4 show respectively the period and dispersion measure distribution of the discovered pulsars overlayed with the global pulsars' population. For comparing the shapes of the distributions, both histograms are normalised at the total number of pulsars in the sample.

Inspecting the periods plot we can note that, as expected from a survey looking at high latitudes (where the effect of the ISM in broadening the pulses is less severe) and using a fast sampling time (125 μs), the ratio between millisecond and long period pulsars is much higher for the population of the PH survey, devoted to the discovery of fast spinning objects indeed, than for the rest of the population (most of which discovered in galactic plane surveys using longer sampling times). Another difference in the two distributions is the peak of the long period pulsars which appears to be at longer periods for the

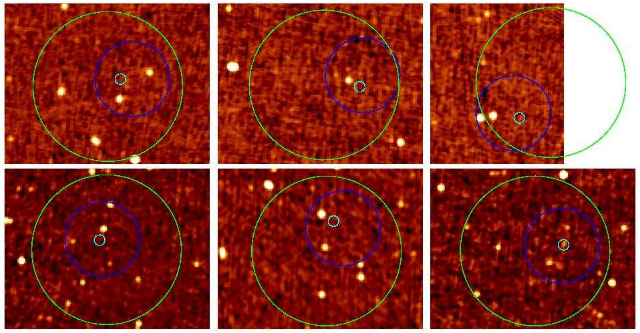

Figure 3.3: Discovery (green), gridding (blue) and timing (cyan, with an error circle increased for graphical purposes) positions on the NVSS maps at 1.4 GHz. From left top corner: J0610−2100, J0656−2228, J0719−2544, J0818−3232, J0820−3921 and J0900−3144. Note the detection of PSR J0900−3144 (see §3.2.2) and possibly of J0719−2544.

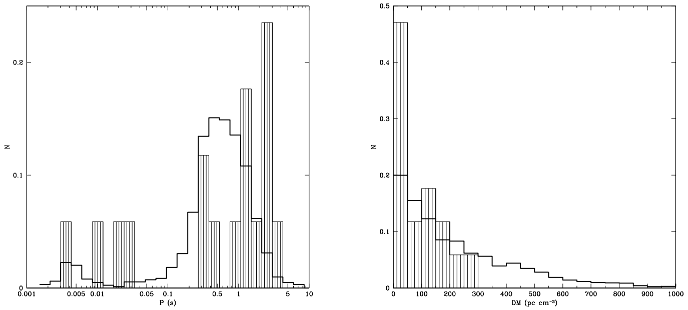

Figure 3.4: Left and right panels show respectively period and DM distributions of new pulsars (shaded region) overlayed with the global pulsar population (thick line). The curves are normalised at the total pulsar number in each sample.

High-Latitude survey than for the overall population. This could be simply an effect of the small number of objects in our sample but it may also reflect a real effect: at high latitudes, hence possibly far from the galactic plane, the pulsars are expected to be older (hence with longer spin periods) having had the time to move far from their birthplaces in the galactic disk. It is also interesting to note that two over four recycled pulsars found in the PH survey have periods above ~ 20 ms placing them in a poorly populated zone of the $P - \dot{P}$ diagram (see fig. 3.6). Millisecond pulsars with these periods are believed to have been

the data span covered and the fit RMS are listed. The parameters reported are basically the ones listed in table 3.5. For this pulsar the eccentricity e, the longitude of periastron ω and the time of periastron $T0$ have been also fitted and are reported in table.

PSR	J0900−3144
RAJ	09:00:43.95251(15)
DECJ	−31:44:30.913(4)
PEPOCH (MJD)	52800.00000
P (s)	0.011109649156558121(16)
$\dot{P}$	$4.82(7) \times 10^{-20}$
DM (pc/cm^3)	75.694(4)
P_b (d)	18.73763572(5)
$a \sin i$ (lt-s)	17.248813(4)
e	$1.05(4) \times 10^{-5}$
ω (°)	70.2(19)
$T0$ (MJD)	52682.28(10)
NTOA	231
SPAN MJD	52599.940 – 53052.450
RMS (μs)	38.275

Table 3.6: Timing parameters for the binary millisecond pulsar J0900−3144. For a description of each parameter see caption of table 3.5 and text.

Timing residuals for PSR J0900−3144, plotted against time (in MJD, top panel) and orbital phase (bottom panel) are shown in figure 3.20, where the blue points with small error bars are the 20 cm Parkes data while the green and the yellow ones are Jodrell Bank data at 20 and 50 cm respectively.

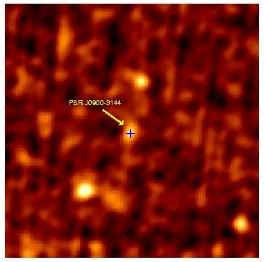

Figure 3.18: NVSS map @1.4 GHz. The blue cross indicates J0900−3144 position.

As mentioned in the caption of figure 3.3, PSR J0900−3144 has been identified in the NVSS map at 1.4 GHz (see fig. 3.18 for a closer view). The position of the point source in the NVSS map is in fact RAJ 09 00 43.92(37),

is a very light star remnant, either a white dwarf or a non degenerate almost exhausted star.

Often this kind of short period, light companion pulsars (e.g. J0024-7204O, and J0024-7204R, in the globular Cluster 47Tuc, Camilo et al. 2000, or B1957+20, in the galactic field, Arzoumanian, Fruchter & Taylor 1994) show long duration eclipses that are believed to be produced by 'windy' mass loss arising from the ablation of the companion by the pulsar wind (e.g. Kluźniak et al. 1988, Phinney et al. 1988, van den Heuvel & van Paradijs 1988). This model is also invoked to explain the nature of isolated millisecond pulsars whose companion star would have been completely destroyed by pulsars' winds.

At least at 20 cm PSR J0610−2100 doesn't show evidence of eclipses. Before excluding the possibility that its light companion is currently ablated it is worthwhile (and already planned) to observe it at higher frequencies where free-free absorption ($\propto \nu^{-2}$) is more effective: PSR J0024-7204J in 47Tuc, for instance, is clearly visible at all orbital phases at 20 cm (Camilo et al 2000) but it shows large eclipses at 70 and 50 cm (Robinson et al. 1995).

Also an optical follow-up will help in better understanding the nature of this binary system: the ablation process implies that the side of the companion facing the pulsar should be heated by the interaction with the pulsar wind and this should be observable in the optical light curves. Hubble Space Telescope (HST) observations would be the best way to test this scenario allowing detection at different orbital phases of such a faint (probably $\sim$ 24 mag on the irradiated side and $\sim$ 26 on the 'dark' side) object.

3.2.2 PSR J0900-3144

PSR J0900−3144 is a binary millisecond pulsar with a spin period of 11.1 ms and an orbital period of 18.7 days. Timing of this object has been performed both with the Parkes Radio telescope, using a central frequency of 1390 MHz, and with the Lovel telescope, a 76 m antenna located in Jodrell Bank, near Manchester (UK). For the latter instrument the observations have been done at 1396 MHz and more recently also at 610 MHz. As for PSR J0610−2100, having multifrequency observations allowed us to obtain a more precise measurement of the dispersion measure.

In table 3.6 the spin and orbital parameters for PSR J0900−3144 are given. In the bottom section of the same table the number of timing points,

spun-up by accreting matter from an intermediate or high mass companion (see §3.3 and §4.2 for the full description of these two pulsars).

The dispersion measure distribution of our pulsars is narrower than the global one. This is not surprising since the interstellar medium in the selected region of the sky, at high latitudes and in the third quadrant of galactic longitudes, is supposed to have a much smaller maximum column density than along the galactic plane.

PSR J	B (G)	τ (Myr)	$\dot{E}$ (erg/s)	d (kpc)	z (kpc)
0343−3000	–	–	–	2.11	< -1.5
0610−2100	2.55×10^{08}	3700	1.1×10^{34}	5.64	< -1.5
0636−4549	2.55×10^{12}	9.844	1.6×10^{31}	1.28	−0.471
0656−2228	–	–	–	2.39	−0.374
0719−2544	2.70×10^{12}	2.120	3.1×10^{32}	17.3	< -1.5
0726−2619	–	–	–	5.46	−0.443
0737−3039A	6.38×10^{09}	205.3	5.9×10^{33}	0.569	−0.0447
0737−3039B	1.58×10^{12}	49.94	1.6×10^{30}	0.568	−0.0446
0746−4529	6.92×10^{12}	2.640	3.0×10^{31}	10	< -1.5
0818−3232	1.29×10^{12}	45.39	3.0×10^{30}	4.2	0.137
0820−3921	3.66×10^{12}	1.397	3.9×10^{32}	7	−0.193
0821−4221	1.19×10^{12}	1.808	2.2×10^{30}	16.9	−0.924
0838−2623	–	–	–	4.92	0.767
0843+0719	–	–	–	3.72	> 1.5
0900−3144	7.41×10^{08}	3600	1.4×10^{30}	0.822	0.135
1038+0034	–	–	–	2.36	> 1.5
1046+0301	–	–	–	2.25	> 1.5

Table 3.3: Derived parameters for the discovered pulsars. Columns give the pulsar name, estimated surface magnetic field, age and spin-down energy, distance from the Sun and height on the galactic plane. For the pulsar outside the Galaxy electronic layer, the Taylor & Cordes model gives only a lower limit on the height.

For pulsars having a measured value of the period derivative, using equations 1.2, 1.3 and 1.6, one can estimate spin-down energies, surface magnetic fields and characteristic ages. These parameters are given in table 3.3 for the pulsars with a coherent timing solution over more than a year. For all new pulsars the distance d from the Sun and the height z on the galactic plane, derived from the DM applying the Taylor & Cordes (1993) model, are also listed. The two latter values, due to the uncertainties in the model of the electron component of the ISM, are known with an intrinsic error of about 30%. Moreover, the estimate of the height on the galactic plane is greatly uncertain for objects beyond the so-called electronic layer, the region of the Galaxy having a scale height of roughly 1.5 kpc, within which the electron

component of the ISM is thicker and beyond which its density rapidly drops becoming comparable with that of the intergalactic medium (Taylor & Cordes 1993). The height values given by the Taylor & Cordes model for pulsars outside the layer are hence only lower limits.

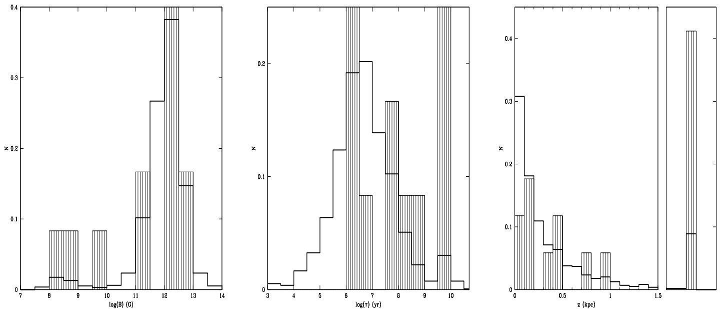

Figure 3.5: From left to right, panels show respectively surface magnetic field, characteristic age and height on the galactic plane distributions of new pulsars (shaded region) overlayed with the global pulsar population (thick line). The curves are normalised at the total pulsar number in each sample. The rightmost part of the height histogram represents the total normalised number of objects for which only lower limits on $|z|$ are available.

The distributions of magnetic fields, ages and heights on the galactic plane of High-Latitude survey pulsars (dashed region) compared with those of the entire population (thick line) are plotted in figure 3.5. The magnetic field histogram (left panel), showing an higher ratio between low and high-field for the PH survey pulsars than for the global population, confirms, as already inferred from the period distribution, the success of the present survey in finding recycled objects. In the age distribution histogram (central panel), we note a lack of young pulsars, again in line with what expected from a survey covering sky regions away from the galactic plane, the likely birthplace of these objects. In the right plot, showing the height distribution on the plane of the Galaxy, the pulsars for which it has been possible to give only a lower limit to $|z|$, are plotted in the rightmost panel: it's clear that our sample is much more spread in galactic height.

The information given in tables 3.2 and 3.3 are graphically summarised in the $P-\dot{P}$ diagram of figure 3.6 where the new pulsars for which a measurement of $\dot{P}$ has been obtained are plotted as red stars (the other points are all the

allowed to fit also for the dispersion measure. No systematic trends are seen in either of the plots, indicating that the orbital solution is correct.

Using equation 2.8 and assuming a standard value for the neutron star mass (typically 1.35 $M_\odot$; Thorsett & Chakrabarty 1999), it's possible to derive an estimate of the minimum companion mass (assuming an edge on orbit). To have a better idea of the possible companion mass range one can plot the mass function in a mass-mass diagram (fig. 3.17) with the mass of the pulsar on the horizontal axis and the mass of the companion on the vertical axis. In §4 we will see how this kind of plot can be used to accurately determine the masses of the stars in a binary system when also post-keplerian parameters are measured.

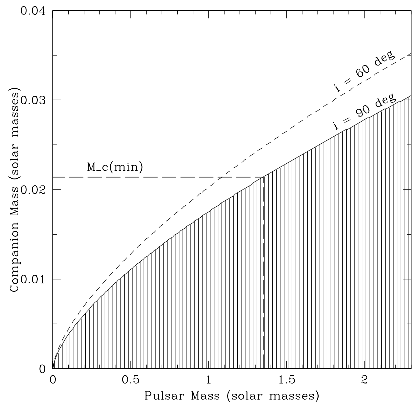

Figure 3.17: Mass-mass diagram for PSR J0610−2100. The shaded region is ruled out by the mass function (simply imposing that the sine of the orbital inclination is greater than one), the dashed curve gives the masses of the two stars for an orbital inclination of 60°. Long-dashed lines indicate the minimum mass companion for a 1.35 $M_\odot$ neutron star.

For PSR J0610−2100 the mass function is $M_f = 0.0000052096(7)\ M_\odot$ giving a companion mass $M_c \geq 0.0214$ for an edge on orbit and assuming $M_{NS} = 1.35\ M_\odot$. Allowing the neutron star mass to vary in the range 1.25 – 1.45 $M_\odot$ and adopting the mean inclination of the orbital plane with respect to the line of sight (i.e. 60°), the companion mass ranges from 0.0235 to 0.0259 $M_\odot$. On the basis of these calculations we can then argue that the companion

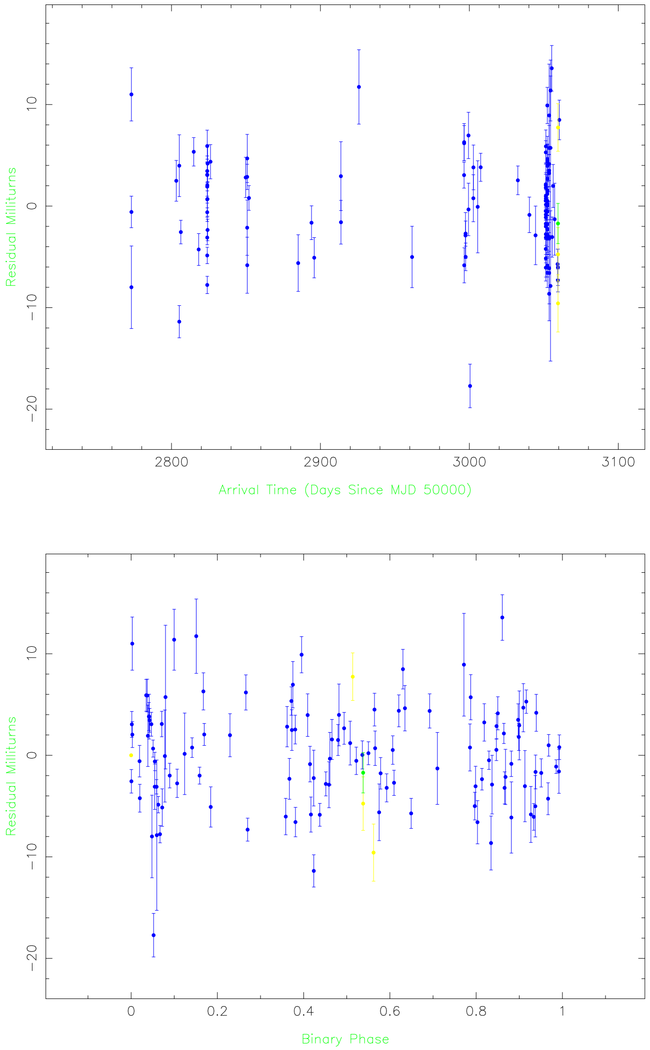

Figure 3.16: Timing residuals. Top panel shows residuals versus time (in MJD) and bottom panel, versus orbital phase. Blue points have been observed at 20 cm, green points at 50 cm and yellow points at 10 cm.

previously known pulsars).

Figure 3.7 shows, for 12 of the 17 new pulsars, the standard profiles used to obtain the times of arrival from convolution with the integrated pulse profiles of each timing point (see §2.3). Pulsars' names, periods an dispersion measures are indicated on each panel. The five remaining pulsars have only few good timing data hence it hasn't yet been produced a good mean profile for them.

Plots from 3.8 to 3.15 show the timing residuals for 8 pulsars (for the millisecond pulsars and the double PSR see following sections; the remaining four pulsars have not yet a coherent timing solution). Root mean square (RMS) of the best fit is indicated on top of each plot along with the provisional pulsar name and period. For PSRs J0818−3232, J0820−3921 and J0821−4221 the residuals improve (roughly by 10%) fitting also the period second derivative. This parameter is much higher than the one predicted by the spin-down law and can only be used as an indicator of the level of timing noise (see 2.3.1) of a pulsar.

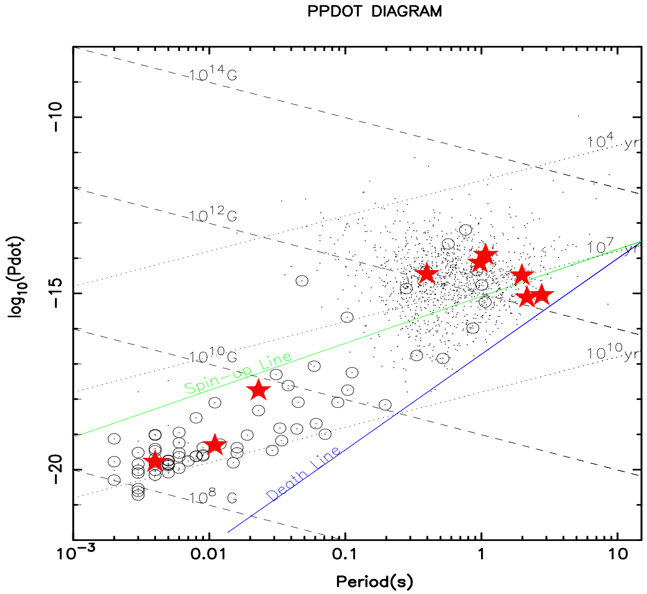

Figure 3.6: Red stars are the new pulsars discovered in the Parkes High-Latitude survey having a coherent timing solution over more than a year. For the description of the lines in the diagram see fig. 1.1 caption.

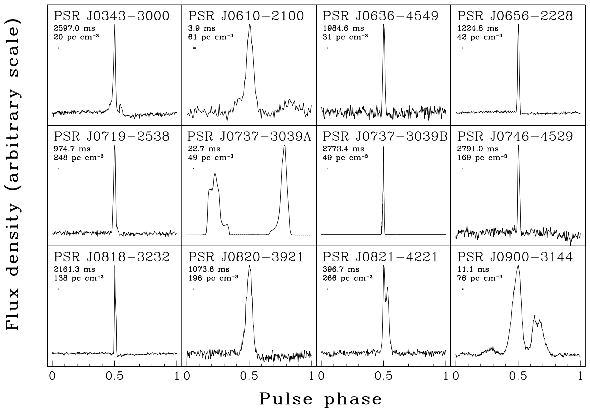

Figure 3.7: Mean 1374 MHz pulse profiles obtained for 12 newly discovered pulsars. For each profile pulsar name, period in milliseconds and dispersion measure are given. The short line (often appearing as a dot) is the time resolution of the profiles.

In table 3.4 the timing data and results for the long period pulsars discovered in the Parkes High-Latitude survey are summarised: first column lists the name of the pulsars, second and third give the number of observations and the time span, in MJD, covered by the timing data used in the fit and fourth and fifth columns reports the residuals of the best fit in microseconds and milliturns (where a turn is the period of the pulsar) respectively.

PSR J	N_{TOA}	Data span (MJD)	Residuals (μs)	Residuals (milliturns)
0343−3000	33	52582 – 53055	1715.008	0.66
0636−4549	45	52393 – 53052	3623.274	1.83
0656−2228	51	52666 – 53052	1201.923	0.98
0719−2544	27	52692 – 53055	194.527	0.19
0746−4529	28	52573 – 53052	2384.478	0.85
0818−3232	52	51866 – 53052	637.101	0.29
0820−3921	49	52309 – 53052	3720.295	3.46
0821−4221	45	52257 – 53052	322.679	0.81

Table 3.4: Summary of timing data and results for long period pulsars having a coherent solution.

3.2 The New Binary Pulsars

Three binary millisecond pulsars have been found in the Parkes High-Latitude Pulsar Survey. In this section the characteristic of two of them, PSR J0610−2100 and PSR J0900−3144, are presented. For the description of the third system see §4.

3.2.1 PSR J0610−2100

PSR J0610−2100 is a 3.8 ms pulsar included in a binary system with an orbital period of 6.8 hr. Table 3.5 (see caption for the description of each entry) gives the spin and orbital parameters obtained by the best fit of the observed times of arrival of the pulses using a keplerian model (BT model, Blandford & Teukolsky 1976). As before, the numbers in parentheses are the 2-σ errors on the last quoted digit(s). Having timing data over little less than a year, spin period, position and period derivative are still covariant in our solution; the errors quoted for these parameters are at 5-σ confidence level.

PSR	J0610−2100
RAJ	06:10:13.591(4)
DECJ	−21:00:28.03(3)
PEPOCH	52920.00000
P (s)	0.00386132470409(17)
$\dot{P}$	$1.5(9) \times 10^{-20}$
DM (pc/cm^3)	60.663(6)
P_b (d)	0.286016000(10)
$a \sin i$ (lt-s)	0.073491(7)
$TASC$ (MJD)	52814.249432(7)
NTOA	119
SPAN MJD	52773.065 –53060.402
RMS (μs)	19.670

Table 3.5: Measured parameters for J0610−2100. From top to bottom: pulsar name, right ascension, declination, reference epoch for the listed period, period, period derivative, dispersion measure, orbital period (in days), projected semi-major axis (in light seconds), time of passage at the ascending node; number of times of arrival used for the fit, data span covered, residuals of the fit in microseconds.

Figure 3.16 shows the timing residuals in milliturns (where a turn is the period of the pulsar) for J0610−2100. In the top panel residuals are plotted versus the time (in MJD) and in bottom panel, versus the binary phase. Blue points are data collected using a central frequency of 1390 MHz (20 cm) while green and yellow points are observations recently taken, respectively, at 50 and 10 cm (680 and 3030 MHz). Having timing data at different frequencies

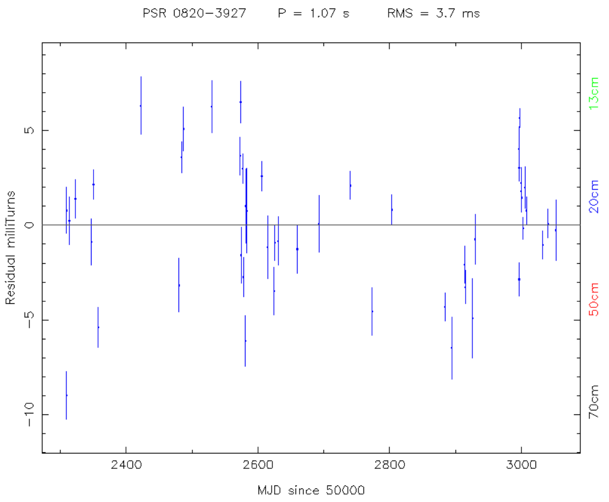

Figure 3.14: Timing residuals for PSR J0820−3921.

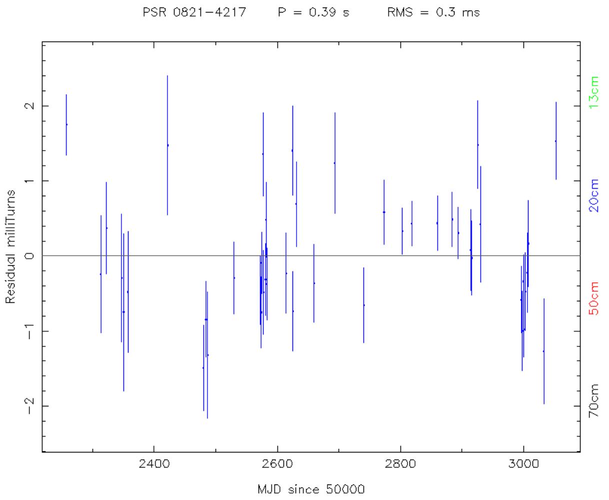

Figure 3.15: Timing residuals for PSR J0821−4221.

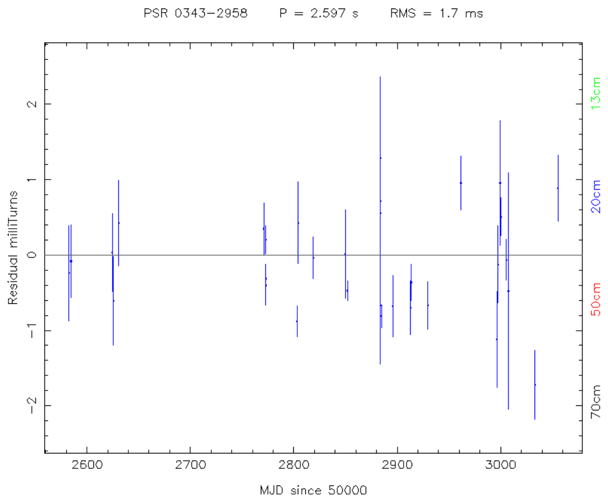

Figure 3.8: Timing residuals for PSR J0343−3000.

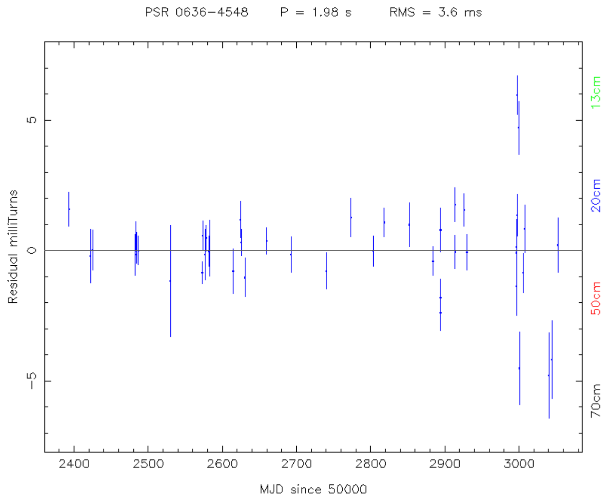

Figure 3.9: Timing residuals for PSR J0636−4549.

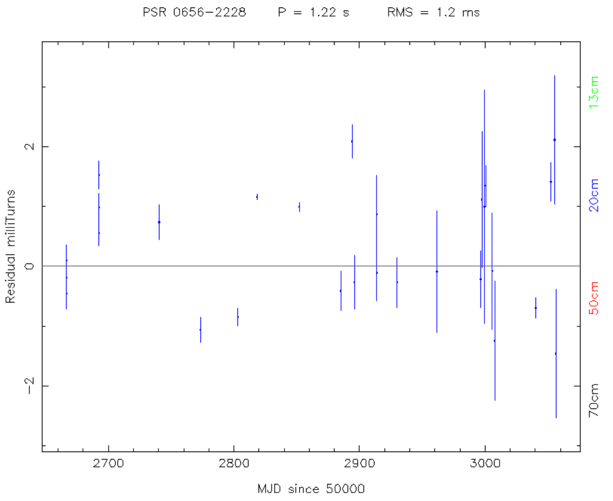

Figure 3.10: Timing residuals for PSR J0656−2228.

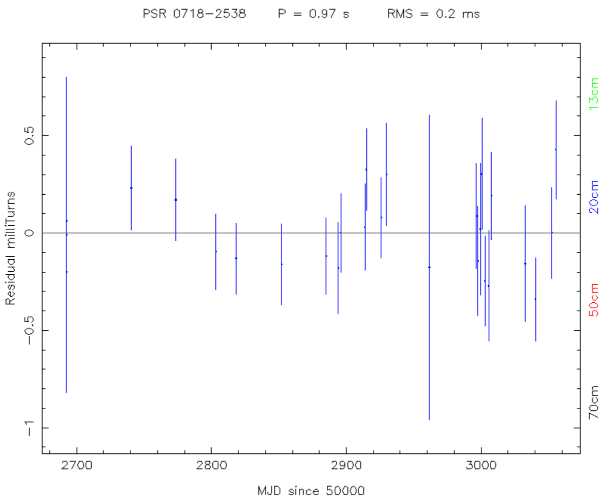

Figure 3.11: Timing residuals for PSR J0719−2544. There is still covariance between period, period derivative and position in the total fit.

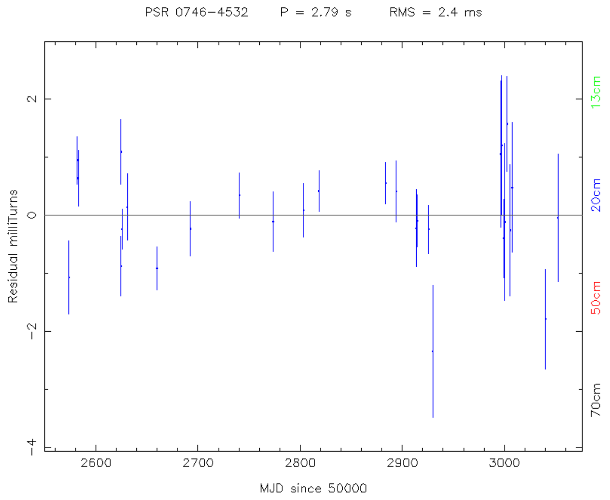

Figure 3.12: Timing residuals for PSR J0746−4529.

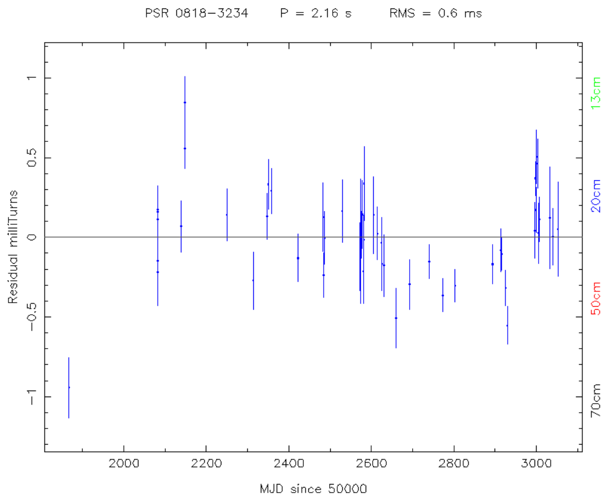

Figure 3.13: Timing residuals for PSR J0818−3232.